

Article

A large West Antarctic Ice Sheet explains early Neogene sea-level amplitude

<https://doi.org/10.1038/s41586-021-04148-0>

Received: 20 January 2021

Accepted: 14 October 2021

Published online: 15 December 2021

 Check for updates

J. W. Marschalek¹✉, L. Zurli², F. Talarico^{2,42}, T. van de Flierdt¹, P. Vermeesch³, A. Carter⁴, F. Beny⁵, V. Bout-Roumazeilles⁵, F. Sangiorgi⁶, S. R. Hemming⁷, L. F. Pérez^{8,9}, F. Colleoni¹⁰, J. G. Preble¹¹, T. E. van Peer^{3,12}, M. Perotti², A. E. Shevenell¹³, I. Browne¹³, D. K. Kulhanek^{14,15}, R. Levy^{11,16}, D. Harwood¹⁷, N. B. Sullivan¹⁸, S. R. Meyers¹⁸, E. M. Griffith¹⁹, C.-D. Hillenbrand⁸, E. Gasson²⁰, M. J. Siegert^{1,21}, B. Keisling⁷, K. J. Licht²², G. Kuhn²³, J. P. Dodd²⁴, C. Boshuis⁶, L. De Santis¹⁰, R. M. McKay¹⁶ & IODP Expedition 374*

Early to Middle Miocene sea-level oscillations of approximately 40–60 m estimated from far-field records^{1–3} are interpreted to reflect the loss of virtually all East Antarctic ice during peak warmth². This contrasts with ice-sheet model experiments suggesting most terrestrial ice in East Antarctica was retained even during the warmest intervals of the Middle Miocene^{4,5}. Data and model outputs can be reconciled if a large West Antarctic Ice Sheet (WAIS) existed and expanded across most of the outer continental shelf during the Early Miocene, accounting for maximum ice-sheet volumes. Here we provide the earliest geological evidence proving large WAIS expansions occurred during the Early Miocene (~17.72–17.40 Ma). Geochemical and petrographic data show glacimarine sediments recovered at International Ocean Discovery Program (IODP) Site U1521 in the central Ross Sea derive from West Antarctica, requiring the presence of a WAIS covering most of the Ross Sea continental shelf. Seismic, lithological and palynological data reveal the intermittent proximity of grounded ice to Site U1521. The erosion rate calculated from this sediment package greatly exceeds the long-term mean, implying rapid erosion of West Antarctica. This interval therefore captures a key step in the genesis of a marine-based WAIS and a tipping point in Antarctic ice-sheet evolution.

Reconstructing past Antarctic ice sheet change informs predictions of the continent's contribution to future sea-level rise^{6,7}. Since the 1970 s, drilling efforts proximal to Antarctica have revealed the general Cenozoic evolution of Antarctic glaciation^{8–11}, but fundamental steps in the development of the ice sheets remain poorly constrained. One key uncertainty is the timing of West Antarctic Ice Sheet (WAIS) initiation and expansion across the outer continental shelf. Deep-sea benthic foraminifer oxygen isotope records and Antarctic abyssal plain sedimentary sequences suggested WAIS formation occurred in the Late Miocene or early Pliocene^{12,13}. However, drilling from the Antarctic margin^{11,14,15} and ice-sheet modelling studies^{4,5,16} have raised the possibility that WAIS expansions into areas below sea-level could have occurred during the Early Miocene or earlier, facilitated by a subaerial West Antarctic topography^{17,18}.

Without widespread WAIS expansions across the continental shelf in the Early Miocene, maximum ice volumes are low enough that global

sea-level fluctuations of ~40–60 m estimated from far-field stratigraphic records¹ and oxygen isotope-derived ice volume estimates^{2,3} require the near complete loss of the East Antarctic Ice Sheet (EAIS) during the warmest Middle Miocene periods². Such an outcome is incompatible with current ice-sheet model outputs, which suggest retention of most terrestrial East Antarctic ice even during the warmest feasible Middle Miocene environmental conditions⁴. This is mainly due to hysteresis effects driven by height–mass balance feedbacks; once the ice sheet is present, parts of it can be retained in a climate warmer than that which would permit ice-sheet inception on an ice-free landscape^{4,19}.

Marine sediments, deposited on the continental shelf of the Ross Sea, can reveal whether the WAIS expanded across the continental shelf during the Early Miocene. However, ice proximal geological records have been hampered by poor recovery, unconformities and/or influence from East Antarctica^{9–11}. Seismic data suggest that significant volumes

¹Department of Earth Science and Engineering, Imperial College London, London, UK. ²Department of Physical, Earth and Environmental Sciences, University of Siena, Siena, Italy. ³Department of Earth Sciences, University College London, London, UK. ⁴Department of Earth and Planetary Sciences, Birkbeck, University of London, London, UK. ⁵Laboratoire d'Océanologie et de Géosciences, UMR 8187 CNRS/Univ Lille/ULCO, Villeneuve d'Ascq, France. ⁶Department of Earth Sciences, Marine Palynology and Paleoceanography, Utrecht University, Utrecht, the Netherlands. ⁷Lamont-Doherty Earth Observatory of Columbia University Palisades, New York, NY, USA. ⁸British Antarctic Survey, Cambridge, UK. ⁹Geological Survey of Denmark and Greenland, Department of Marine Geology, Aarhus, Denmark. ¹⁰National Institute of Oceanography and Applied Geophysics – OGS, Trieste, Italy. ¹¹GNS Science, Lower Hutt, New Zealand. ¹²National Oceanography Centre Southampton, University of Southampton Waterfront Campus, Southampton, UK. ¹³College of Marine Science, University of South Florida, St. Petersburg, FL, USA. ¹⁴International Ocean Discovery Program, Texas A&M University, College Station, TX, USA. ¹⁵Institute of Geosciences, Christian-Albrechts-University of Kiel, Kiel, Germany. ¹⁶Antarctic Research Centre, Victoria University of Wellington, Wellington, New Zealand. ¹⁷Department of Earth and Atmospheric Sciences, University of Nebraska-Lincoln, Lincoln, NE, USA. ¹⁸Department of Geoscience, University of Wisconsin-Madison, Madison, WI, USA. ¹⁹School of Earth Sciences, Ohio State University, Columbus, OH, USA. ²⁰Centre for Geography and Environmental Sciences, University of Exeter, Cornwall, UK. ²¹Grantham Institute, Imperial College London, London, UK. ²²Department of Earth Sciences, Indiana University-Purdue University Indianapolis, Indianapolis, IN, USA. ²³Alfred Wegener Institute, Helmholtz Centre for Polar and Marine Research, Bremerhaven, Germany. ²⁴Department of Geology and Environmental Geosciences, Northern Illinois University, DeKalb, IL, USA. ⁴²Deceased: F. Talarico. *A list of authors and their affiliations appears at the end of the paper. [✉]e-mail: j.marschalek18@imperial.ac.uk

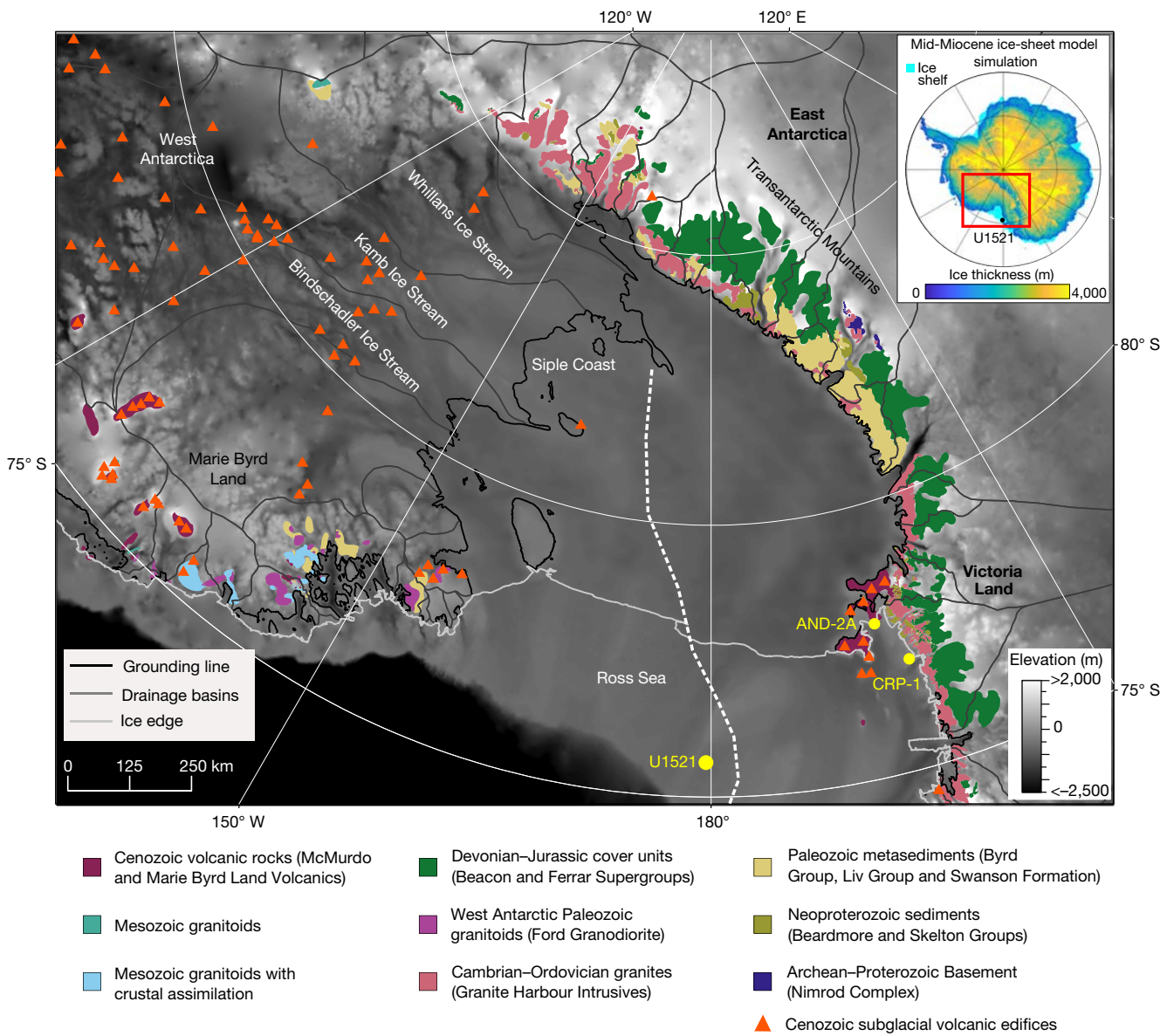


Fig. 1 | Site U1521 location and surrounding geology. The outcropping regional geology around the Ross Sea⁴² (© SCAR GeoMAP and GNS Science 2019) is overlain on the BedMachine Antarctica V1 modern bed topography^{43,44}. The MEASUREs grounding line, ice-sheet margin and basins are used^{45,46} and the map was produced using ArcGIS software. IODP Site U1521 is located on the outer continental shelf of the central Ross Sea. Locations referenced in the text are labelled, including the ANDRILL 2A (AND-2A) and Cape Roberts Project 1 (CRP-1) drill sites. The white dashed line indicates the boundary between East and West

Antarctic lithosphere⁴⁷. Orange triangles show Cenozoic subglacial volcanic edifices detected based on morphological characteristics, gravity anomalies and magnetic anomalies²⁹. The inset shows an ice-sheet model simulation using a ‘cold’ climate (‘cold’ orbit and a climate with 280 ppm atmospheric CO₂ concentrations) and an estimated Middle Miocene topography (inset map reproduced with permission from ref.⁴, PNAS). Provenance indicators from Site U1521 Sequence 2 sediments are broadly consistent with an ice sheet similar to or exceeding the extent of this model output.

of lower Miocene glacimarine sediment exist around the West Antarctic margin^{20–23}. However, seismic data require constraints from drilling to determine the age of the sediments, and to differentiate between detritus from continental-scale ice-sheet expansion and local ice caps on (paleo)topographic highs^{22,23}. Consequently, WAIS grounding across the Ross Sea shelf is only clear in seismic data after the Middle Miocene Climate Transition (~14 Ma)^{24,25}; it remains uncertain whether there were earlier WAIS expansions across the Ross Sea shelf.

IODP Site U1521 and provenance approach

IODP Expedition 374 Site U1521 (75°41.0' S, 179°40.3' W; 562 m water depth) was drilled to 650.1 m below sea floor (mbsf) in the Pennell Basin on the outer continental shelf of the Ross Sea (Fig. 1). The site

was drilled in a region that ice-sheet models indicate is one of the last locations where ice grounds during glacial maxima, making it an ideal location to assess the timing of past WAIS expansions onto the outer continental shelf^{4,16,26}. The sediments from the base of the borehole up to 209.17 mbsf are split into four chronostratigraphic sequences (1–4; Fig. 2), which constitute an expanded lower Miocene section (~18 to ~16.3 Ma; Supplementary Information) with 73% recovery. These sediments provide a unique window for detailed analysis of ice-sheet behaviour immediately before the onset of the Miocene Climate Optimum (MCO, ~17 Ma; Fig. 2; Extended Data Fig. 1; Extended Data Table 1).

Site U1521 sediments below 209.17 mbsf are predominantly muddy to sandy diamictites, often interbedded with thin laminae and beds of mudstone (Supplementary Information)²⁶. Palynological counts on 23 samples revealed sparse palynomorphs in Sequences 1 and 4A,

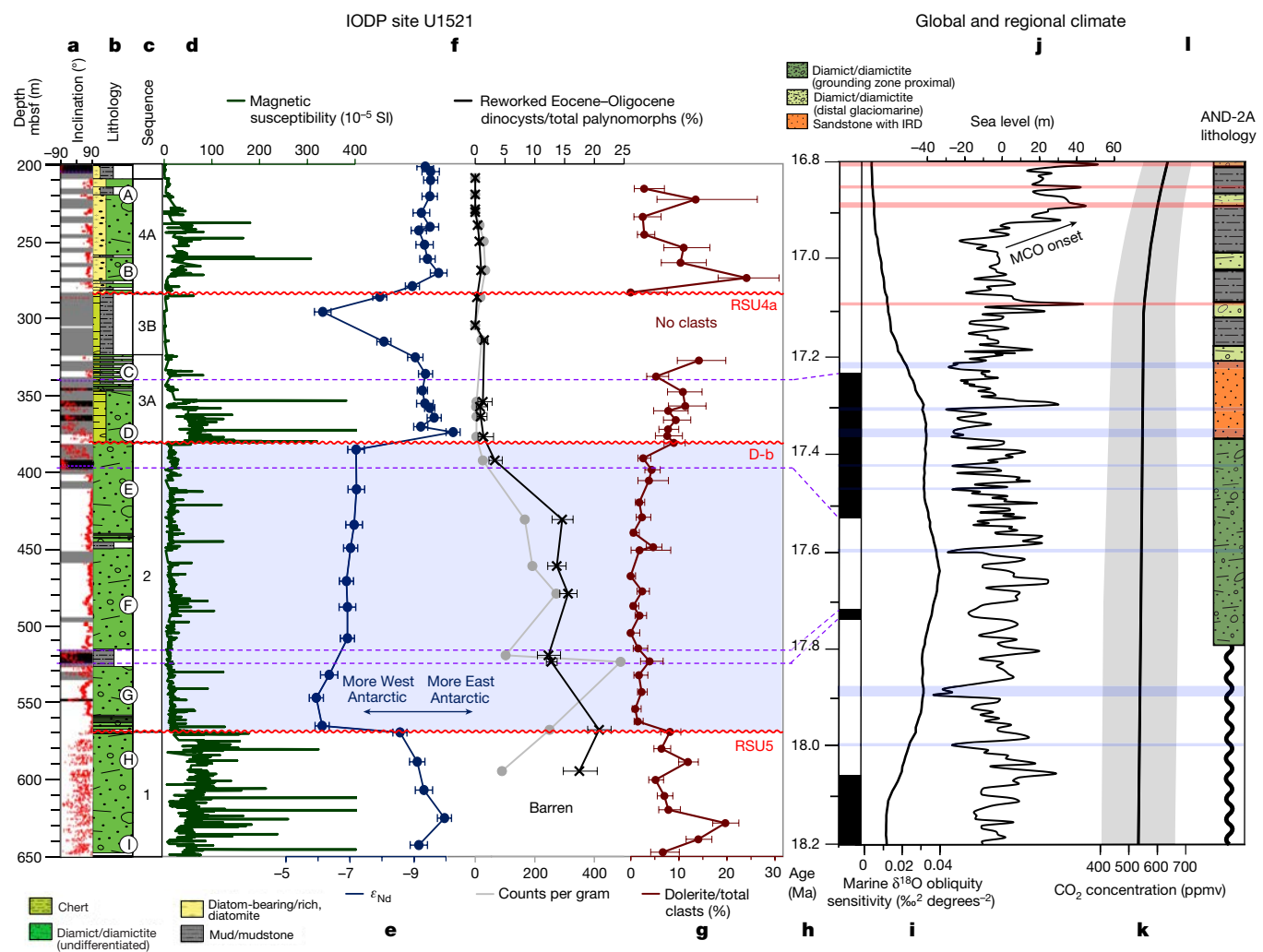


Fig. 2 | Selected provenance proxies from IODP Site U1521 compared with Early Miocene climate records. The light-blue-shaded section (Sequence 2) highlights the interval with sediments of predominantly West Antarctic provenance. The depth of Ross Sea Unconformity (RSU) 4a and 5 and seismic surface D-b are indicated in red²³. **a**, Site U1521 inclination data after 20 mT demagnetization (red points)²⁶ and polarity interpretation (white = reverse polarity, black = normal polarity, grey = no interpretation). **b**, Site U1521 lithostratigraphy²⁶. **c**, Chronostratigraphic sequences. The circled letters between **(b)** and **(c)** mark the depths of the zircon U-Pb samples (Fig. 3). **d**, Magnetic susceptibility measured on the whole core²⁶. **e**, Neodymium isotope signature of the fine fraction. Error bars are 2 s.d. external reproducibility; for provenance interpretations, see Extended Data Fig. 4 and references in Supplementary Information. **f**, Abundance of Eocene–Oligocene dinocysts as a

percentage (black) and concentration (that is, counts per gram of sediment; grey). **g**, Dolerite clast abundance. Errors shown in **(f)** and **(g)** are 95% confidence intervals⁴⁸. Magnetostratigraphic tie points between the polarity interpretations from shipboard data **(a)**²⁶ and geomagnetic polarity timescale **(h)**⁴⁹ are marked by purple dashed lines. **i**, Obliquity sensitivity, indicating the strength of obliquity in the $\delta^{18}\text{O}$ record relative to the theoretical strength of obliquity forcing. This has been interpreted as representing the presence of marine-based Antarctic ice¹⁵. **j**, Sea-level record based on an oxygen isotope splice². Red- and blue-shaded intervals indicate pronounced sea-level highstands (>40 m) and lowstands (<-20 m), respectively. MCO = Miocene Climatic Optimum. **k**, CO₂ reconstruction with a LOESS smoothing (shaded region indicates 1 σ error)⁵⁰. **l**, Simplified lithological log from the AND-2A record, with diamictites differentiated based on a grounding-zone proximal versus distal glacimarine depositional setting^{11,15}.

common reworked dinoflagellate cysts in Sequence 2, and evidence for high biological productivity in Sequence 3B (Extended Data Fig. 2; Supplementary Information). These lithological and paleontological data from Sequences 1, 2, 3A and 4A indicate an ice-proximal glacimarine (and potentially subglacial) setting, while data from Sequence 3B suggest an ice-distal setting. Notably, the ~190-m-thick succession of Sequence 2, containing a high proportion of reworked dinoflagellate cysts, was deposited rapidly (0.592 mm yr⁻¹) within a ~317 kyr interval spanning -17.72–17.40 Ma (Extended Data Fig. 1).

Through comparison with terrestrial rock outcrops, the sediments recovered at Site U1521 were traced back to their source regions. A differing geological history of the rocks beneath the EAIS and WAIS (Fig. 1) gives the sediment eroded by each ice sheet a distinct geochemical, petrological and mineralogical composition, allowing expansions of the EAIS and WAIS to be distinguished. To avoid bias towards, or omission

of, any lithologies, we applied multiple sediment provenance proxies²⁷. Specifically, we analysed the detrital fine fraction of 37 samples for neodymium (Nd) and strontium (Sr) isotope compositions (<63 μm) and 23 samples for clay mineralogy (<2 μm). Nine samples were also processed for U-Pb dating of detrital zircons (<300 μm) and five for ⁴⁰Ar/³⁹Ar dating of detrital hornblende grains (150–300 μm). Additionally, the petrological composition of 15,740 clasts >2 mm was identified down-core (Extended Data Fig. 3).

Evidence for Early Miocene WAIS growth

At Site U1521, detrital ε_{Nd} values are consistently more radiogenic (higher) in Sequence 2 compared with the sediments above and below (Fig. 2e), implying a contribution from a more radiogenic end member. This end member can be traced to beneath the WAIS; the ε_{Nd} values, ranging between -7.2

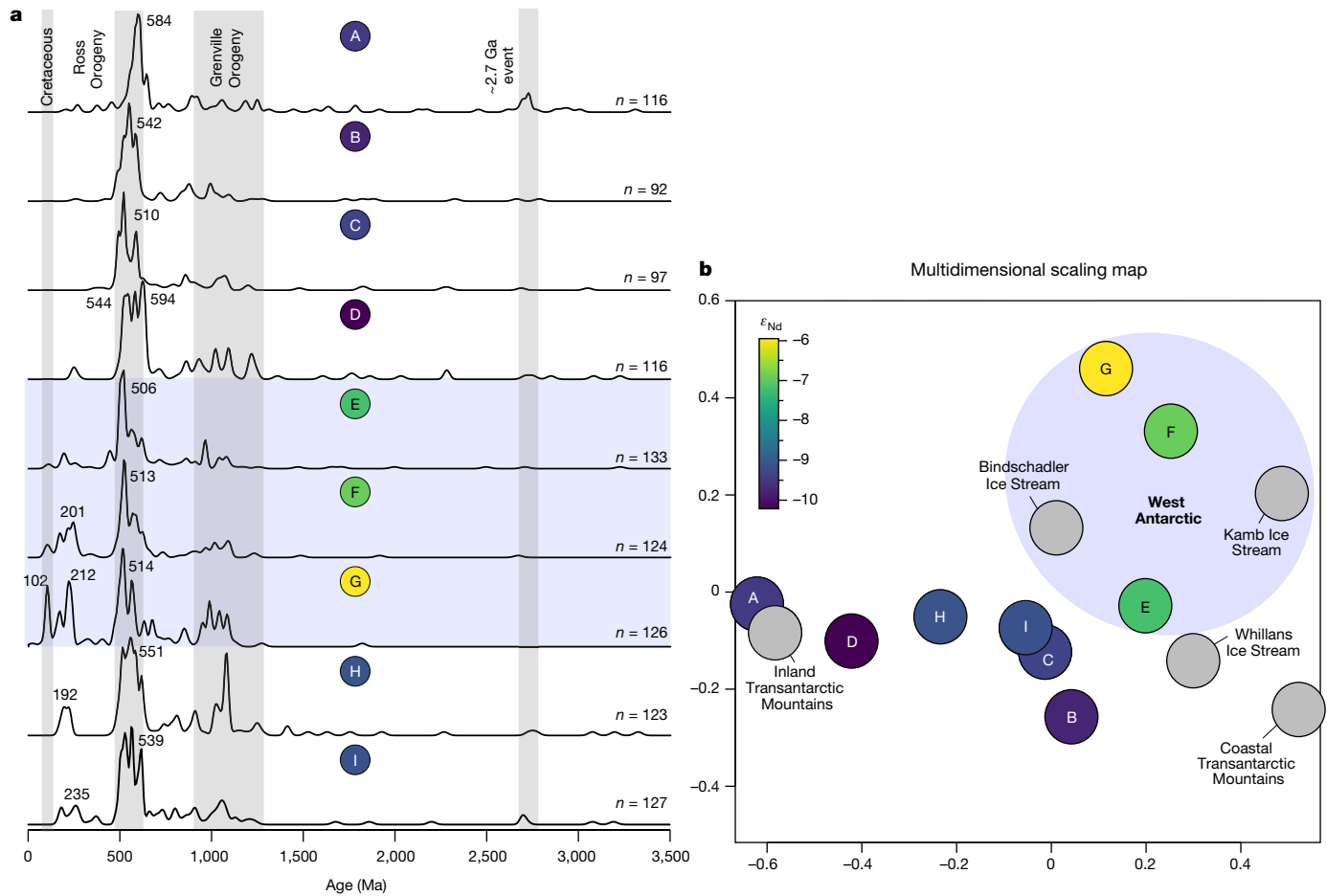


Fig. 3 | Site U1521 detrital zircon U-Pb age distributions. a, Data displayed as kernel density estimates (KDEs). When present, large Ross Orogeny (-600–500 Ma), Triassic (-240–190 Ma) and Cretaceous (-100 Ma) age peaks are labelled. The age ranges of the Ross Orogeny, Grenville Orogeny and an -2.7 Ga event recorded in Ross Sea sedimentary strata are illustrated using grey-shaded bars. The sub-bottom depth midpoints of the samples are shown in Fig. 2 and listed in the Methods section. **b,** Same data as in (a), displayed as a multidimensional scaling (MDS) map calculated using the Kolmogorov–Smirnov statistic⁵¹. Stress (a measurement of the goodness of fit between the disparities and the fitted distances⁵¹) = 0.072. An MDS plot visualizes the degree of similarity between samples, with the proximity of sample points

reflecting their similarity. The axis scales are dimensionless and have no physical meaning. The colour of Site U1521 samples (A to I) corresponds to their ε_{Nd} value. Previously published zircon U-Pb data from Kamb, Whillans and Bindschadler ice streams in West Antarctica, as well as Transantarctic Mountain moraines from inland and coastal regions, are shown in grey^{32–34}. The KDEs and region of the MDS plot interpreted as having a West Antarctic provenance are shaded in light blue, consistent with the blue shading in panel (a) and Fig. 2. Note that although Whillans Ice Stream drains the WAIS, it is excluded from the blue-shaded area due to its proximity to the Transantarctic Mountains (Fig. 1), resulting in a subglacial sediment provenance signature indistinguishable from East Antarctic detritus³³.

and -5.9, are in good agreement with measurements of Upper Quaternary diamictic from the eastern Ross Sea shelf, adjacent to West Antarctica²⁸. Here, the radiogenic end member is hypothesized to be the Cenozoic alkali volcanic rocks of Marie Byrd Land, West Antarctica (Extended Data Fig. 4)²⁸. Subaerial outcrops of the Marie Byrd Land volcanic province are limited, but magnetic and gravity anomalies associated with subglacial cone-shaped structures indicate the presence of numerous subglacial volcanoes (Fig. 1)²⁹. We hypothesize that the Marie Byrd Land volcanic province is the more radiogenic end member in Sequence 2. Conversely, the less radiogenic (lower) ε_{Nd} values seen in Sequences 1, 3A and 4A reflect a mixture of lithologies present in the (East Antarctic) Transantarctic Mountains and fall within the range of Upper Quaternary Ross Sea till sediments of Transantarctic Mountain provenance (Extended Data Figs. 4, 5)^{28,30}. These less radiogenic sediments also show higher and more variable magnetic susceptibility (Fig. 2)²⁶. The patterns seen in the ε_{Nd} data are broadly mirrored by detrital Sr isotope compositions (Extended Data Fig. 2).

Single-grain geochronology/thermochronology and clast petrography provide insights into specific source terranes. In the Transantarctic Mountains, Precambrian rocks were affected by the pervasive Ross Orogeny (615–470 Ma), which was accompanied by intrusive felsic magmatism

(Supplementary Information)³¹. Zircon age populations from Sequences 1, 3A and 4A show a strong peak towards the earlier part of the Ross Orogeny (595 to 535 Ma) and a 6 to 21% population of Archaean and Paleoproterozoic (>1,600 Ma) zircon grains (Figs. 1, 3). These features, together with a lack of grains younger than 250 Ma, resemble data from moraines in the Transantarctic Mountains^{32–34}. Clasts in sequences 1, 3A and 4A also correlate with rocks in the Transantarctic Mountains, with lithologies including common felsic granitoids and meta-sediments alongside rarer limestones, marbles and sandstones (Extended Data Fig. 3)³¹. Although a relatively minor component, dolerite clasts are found throughout Sequences 1, 3A and 4A (Fig. 2g) and can be traced to the Jurassic Ferrar Group, which predominantly crops out in the Transantarctic Mountains (Fig. 1). Furthermore, rare *Protohaploxylinus* pollen, a distinctive component of the Permian Beacon Supergroup in the Transantarctic Mountains, are observed in Sequence 3A³⁵. Overall, the sediments comprising Site U1521 Sequences 1, 3A and 4A are predominantly sourced from erosion of the Transantarctic Mountains in East Antarctica.

In contrast, Sequence 2 is characterized by the highest ε_{Nd} values and contains zircons with Cretaceous (-100 Ma) U-Pb ages ($n = 16$; Fig. 3a). Such ages are indicative of a West Antarctic provenance as they

Article

are currently only found beneath the modern Siple Coast ice streams, including Kamb Ice Stream and those closer to Marie Byrd Land^{33,36}. The age spectra of samples from Sequence 2 share other features with data from the Siple Coast ice streams, including a broad Triassic (-240–190 Ma) age peak, few pre-Mesoproterozoic zircons (<5% of grains) and a young (-515–505 Ma) Ross Orogeny peak (Fig. 3)³³. Detrital hornblende $^{40}\text{Ar}/^{39}\text{Ar}$ ages from Sequence 2 further corroborate a West Antarctic provenance. Unlike zircon grains, which can survive multiple sedimentary cycles, hornblende grains are less resistant to weathering. The absence of Grenvillian (-1,100–900 Ma) ages in the Sequence 2 hornblende sample (Extended Data Fig. 6) therefore suggests a West Antarctic provenance, as Grenville-age rocks are absent there³⁷. The scarcity of Ferrar Group dolerite clasts, common in the Transantarctic Mountains, is also consistent with a West Antarctic provenance (Figs. 1, 2), as is a high proportion of smectite in the clay fraction at the bottom of Sequence 2 ($\leq 58\%$; Extended Data Fig. 3), with smectite percentages similar to Quaternary sediments in the eastern Ross Sea³⁸. Additionally, Sequence 2 contains evidence for recycling of older marine detritus, most likely from the lower Cenozoic rift-fill strata that exist in the eastern Ross Sea region of the West Antarctic Rift System²¹. This is inferred from the dominance of reworked Eocene–Oligocene species in the diatom and spore-pollen assemblages²⁶, alongside the common (13–21%) reworked Eocene–Oligocene marine dinocysts, which are rare (<1.5%) in younger sediments (Extended Data Fig. 2).

Smectite abundance declines significantly up-section within Sequence 2 and is accompanied by an increase in the proportion of basalt clasts (Extended Data Fig. 7). This anticorrelation is unexpected given that smectite is a weathering product of basalt and volcanic rocks. We infer that lower in Sequence 2, basaltic bedrock was predominantly weathered to smectite and was thus largely confined to the finer grain size fractions. Over time, this more weathered regolith layer was removed, leading to erosion of progressively more pristine continental detritus containing more basalt clasts. This scenario is supported by more radiogenic ε_{Nd} values measured in the $<63 \mu\text{m}$ fraction lower in Sequence 2 (Fig. 2, Extended Data Fig. 7), as Marie Byrd Land basalts are more radiogenic than other lithologies (Extended Data Fig. 5). Sequence 2 (17.72–17.40 Ma) could therefore record an advance of the WAIS over parts of West Antarctica that had not been covered by grounded ice for an extended period.

Further evidence for WAIS expansion can be found in seismic data, which can trace the sediment package deposited at Site U1521 between 17.72 and 17.40 Ma (Sequence 2) across the Ross Sea continental shelf²³. The sediment package, which is thicker towards the eastern Ross Sea (that is, West Antarctica), contains glacial features including widespread progradational wedges and high relief morainal banks^{20,21,23}. Coupled with the lithological and palynological evidence for ice proximity at Site U1521, this shows that marine-terminating ice was present. Transport of large volumes of West Antarctic detritus as far west as the Pennell Basin in the central Ross Sea is evident in our provenance data, which, alongside common reworked marine microfossils, proves this marine-terminating ice derived from an Early Miocene WAIS, which intermittently extended across most of the outer continental shelf.

Our data therefore reveal WAIS expansions across the Ross Sea continental shelf date back to at least 17.72 Ma, which is significantly earlier than previously suggested^{12,13,23,24,39}. Advance of the WAIS into marine-based areas (that is, regions grounded mainly below sea level) at 17.72–17.40 Ma is supported by a corresponding period of high sensitivity of the marine $\delta^{18}\text{O}$ record to obliquity forcing (Fig. 2i). High obliquity sensitivity is considered a proxy for enhanced ice-sheet sensitivity to ocean dynamics and thus the presence of marine-based ice¹⁵.

Birth of a marine-based WAIS

The mean erosion rate for the WAIS catchments draining to the Ross Sea between 17.72 and 17.40 Ma can be estimated using the volume of

the corresponding seismic package east of Site U1521²³. Assuming that, at the time of deposition, the area of the Ross Sea drainage sector of the WAIS was approximately the same as today ($\pm 20\%$), the inferred sediment volume requires a mean catchment erosion of approximately 87 m in ~317 kyr (Extended Data Table 2). The mean erosion rate of $-0.275 \text{ mm yr}^{-1}$ during this interval greatly exceeds the long-term mean rate of 0.012 mm yr^{-1} calculated for this part of the WAIS between 23 and 14 Ma¹⁸, even when the full uncertainty is taken into account (Extended Data Table 2), it is still more than an order of magnitude higher. This highlights the 17.72 to 17.40 Ma interval as one of unusually rapid erosion, with erosion rates comparable to modern subpolar to temperate glacial catchments⁴⁰. Transporting this large volume of subglacially eroded debris quickly to the WAIS margin required abundant meltwater at the ice sheet bed⁴¹, as well as fast-flowing ice streams that extended into marine settings where broad deposition took place. Ocean temperatures must therefore have been sufficiently cool to permit the advance of marine-based ice, yet atmospheric conditions must have remained warm enough to provide sufficient precipitation to drive dynamic ice flow and enhanced basal erosion⁴.

Since most of West Antarctica, apart from Marie Byrd Land, was thermally subsiding throughout the Miocene¹⁸, the high erosion rate at 17.72 to 17.40 Ma is unlikely to have been driven by tectonic uplift. The eroded sediments therefore reflect ice expansion and enhanced glacial incision of the terrestrial West Antarctic hinterland, plus infilling of the Ross Sea basins. This erosive event occurred at a time when topographic reconstructions indicate a transition from a terrestrial West Antarctic topography (23 Ma) to a largely submarine West Antarctic topography (14 Ma)¹⁸. The timing and large volume of sediment deposited in Sequence 2 at Site U1521 suggests that the 17.72 to 17.40 Ma interval records a critical step in the transition of the WAIS from a largely terrestrial ice sheet to one that was primarily marine-based. This significant alteration to West Antarctic topography occurred just before major changes affecting the Antarctic cryosphere and global climate during the MCO^{2,11}. Subglacial erosion may therefore have driven changes in ice-sheet evolution and behaviour as, after ~17.40 Ma, a greater submarine area in central West Antarctica would have made the mass-balance control of the WAIS more sensitive to external drivers such as sea level and oceanic forcing^{5,16}. We propose that ice retreat at the onset of the MCO may be partially attributable to the crossing of this topographic tipping point and that Sequence 2 records the birth of a marine-based WAIS. This event dates to well before 14 Ma, the time slice at which topographic reconstructions first show a largely sub-marine West Antarctica¹⁸.

Sea-level reconciliation

Grounded ice flowing from West Antarctica was close to Site U1521 towards the end of the Early Miocene. We therefore validate recent modelling studies suggesting that an ice sheet nucleating on a partially terrestrial West Antarctica could expand extensively into the marine realm under Early Miocene climatic and paleotopographic conditions^{4,5,16}. Our data are consistent with an ice extent similar to, or exceeding, the largest modelled Early to Middle Miocene Antarctic ice sheets (Fig. 1), containing ice volumes of approximately 80 m sea-level equivalent depending on the topographic reconstruction used^{4,5,16}. This expanded WAIS contained approximately 14–15 m sea-level equivalent of ice, but also acted to buttress the EAIS resulting in significantly larger-than-present ice volumes^{4,16}. These maximum ice volume constraints indicate that far-field sea-level amplitudes of ~40–60 m did not require the loss of nearly all terrestrial East Antarctic ice during subsequent warm periods during the MCO^{1–3}, consistent with modelled EAIS hysteresis effects⁴. By providing the earliest conclusive evidence for a large marine-based WAIS, our data also dispel long-held inferences that a WAIS, able to significantly impact global eustacy and climate, was not present until the Middle or Late Miocene^{12,13,39}.

Online content

Any methods, additional references, Nature Research reporting summaries, source data, extended data, supplementary information, acknowledgements, peer review information; details of author contributions and competing interests; and statements of data and code availability are available at <https://doi.org/10.1038/s41586-021-04148-0>.

1. Kominz, M. A. et al. Miocene relative sea level on the New Jersey shallow continental shelf and coastal plain derived from one-dimensional backstripping: A case for both eustasy and epeirogeny. *Geosphere* **12**, 1437–1456 (2016).
2. Miller, K. G. et al. Cenozoic sea-level and cryospheric evolution from deep-sea geochemical and continental margin records. *Sci. Adv.* **6**, eaaz1346 (2020).
3. Pekar, S. F. & DeConto, R. M. High-resolution ice-volume estimates for the early Miocene: Evidence for a dynamic ice sheet in Antarctica. *Palaeogeogr. Palaeoclimatol. Palaeoecol.* **231**, 101–109 (2006).
4. Gasson, E., DeConto, R. M., Pollard, D. & Levy, R. H. Dynamic Antarctic ice sheet during the early to mid-Miocene. *Proc. Natl Acad. Sci. USA* **113**, 3459–3464 (2016).
5. Paxman, G. J., Gasson, E. G., Jamieson, S. S., Bentley, M. J., & Ferraccioli, F. Long-term increase in antarctic ice sheet vulnerability driven by bed topography evolution. *Geophys. Res. Lett.* **47**, e2020GL090003 (2020).
6. Masson-Delmotte, V. et al. in *Climate Change 2013: The Physical Science Basis* (eds Stocker, T. F. et al.) 383–464 (IPCC, Cambridge Univ. Press, 2013).
7. Kennicutt, M. C. et al. A roadmap for Antarctic and Southern Ocean science for the next two decades and beyond. *Antarct. Sci.* **27**, 3–18 (2014).
8. Kennett, J. P. Cenozoic evolution of Antarctic glaciation, the circum-Antarctic Ocean, and their impact on global paleoceanography. *J. Geophys. Res.* **82**, 3843–3860 (1977).
9. Barrett, P. J. Characteristics of pebbles from Cenozoic marine glacial sediments in the Ross Sea (DSDP Sites 270–274) and the South Indian Ocean (Site 268). *Initial Rep. Deep Sea Drill. Proj.* **28**, 769–784 (1975).
10. Passchier, S. & Krissel, L. A. Oligocene–Miocene Antarctic continental weathering record and paleoclimatic implications, Cape Roberts drilling project, Ross Sea, Antarctica. *Palaeogeogr. Palaeoclimatol. Palaeoecol.* **260**, 30–40 (2008).
11. Levy, R. et al. Antarctic ice sheet sensitivity to atmospheric CO₂ variations in the early to mid-Miocene. *Proc. Natl Acad. Sci. USA* **113**, 3453–3458 (2016).
12. Zachos, J., Pagani, M., Sloan, L., Thomas, E. & Billups, K. Trends, rhythms, and aberrations in global climate 65 Ma to present. *Science* **292**, 686–693 (2001).
13. Kennett, J. P. & Barker, P. F. Latest Cretaceous to Cenozoic climate and oceanographic developments in the Weddell Sea, Antarctica: an ocean-drilling perspective. *Proc. Ocean Drill. Program, Sci. Results* **113**, 937–960 (1990).
14. Hauptvogel, D. W. & Passchier, S. Early–Middle Miocene (17–14 Ma) Antarctic ice dynamics reconstructed from the heavy mineral provenance in the AND-2A drill core, Ross Sea, Antarctica. *Global Planet. Change* **82**, 38–50 (2012).
15. Levy, R. H. et al. Antarctic ice-sheet sensitivity to obliquity forcing enhanced through ocean connections. *Nat. Geosci.* **12**, 132–137 (2019).
16. Colleoni, F. et al. Past continental shelf evolution increased Antarctic ice sheet sensitivity to climatic conditions. *Sci. Rep.* **8**, 1–12 (2018).
17. Wilson, D. S. et al. Antarctic topography at the Eocene–Oligocene boundary. *Palaeogeogr. Palaeoclimatol. Palaeoecol.* **335–336**, 24–34 (2012).
18. Paxman, G. J. et al. Reconstructions of Antarctic topography since the Eocene–Oligocene boundary. *Palaeogeogr. Palaeoclimatol. Palaeoecol.* **535**, 109346 (2019).
19. Gasson, E. G. & Keisling, B. A. The Antarctic Ice Sheet: A Paleoclimate modelling perspective. *Oceanography (Wash. D.C.)* **33**, 90–100 (2020).
20. Anderson, J. B. & Bartek, L. R. in *The Antarctic Paleoenvironment: A Perspective on Global Change. Part One Vol. 56* (eds Kennett, J.P. & Warkne, D. A.) 231–264 (AGU, 1992).
21. De Santis, L., Anderson, J. B., Brancolini, G. & Zayatz, I. in *Geology and Seismic Stratigraphy of the Antarctic Margin* Vol. 68 (eds Cooper, A. K., Barker, P. F. & Brancolini, G.) 235–260 (AGU, 1995).
22. Gohl, K. et al. Seismic stratigraphic record of the Amundsen Sea Embayment shelf from pre-glacial to recent times: Evidence for a dynamic West Antarctic Ice Sheet. *Mar. Geol.* **344**, 115–131 (2013).
23. Pérez, L. F. et al. Early-middle Miocene ice sheet dynamics in the Ross Sea embayment: results from integrated core-log-seismic interpretation. *Geol. Soc. Am. Bull.* <https://doi.org/10.1130/B35814.1> (2021).
24. Bart, P. J. Were West Antarctic ice sheet grounding events in the Ross Sea a consequence of East Antarctic ice sheet expansion during the middle Miocene? *Earth Planet. Sci. Lett.* **216**, 93–107 (2003).
25. Chow, J. M. & Bart, P. J. West Antarctic Ice Sheet grounding events on the Ross Sea outer continental shelf during the middle Miocene. *Palaeogeogr. Palaeoclimatol. Palaeoecol.* **198**, 169–186 (2003).
26. McKay, R., De Santis, L. & Kulhanek, D. K. and the Expedition 374 Science Party. Ross Sea West Antarctic Ice Sheet History in *Proc. Int. Ocean Discovery Program (IODP, 2019)*.
27. Licht, K. J. & Hemming, S. R. Analysis of Antarctic glaciogenic sediment provenance through geochemical and petrologic applications. *Quat. Sci. Rev.* **164**, 1–24 (2017).
28. Farmer, G. L., Licht, K., Swope, R. J. & Andrews, J. Isotopic constraints on the provenance of fine-grained sediment in LGM tills from the Ross Embayment, Antarctica. *Earth Planet. Sci. Lett.* **249**, 90–107 (2006).
29. van Wyk de Vries, M., Bingham, R. G. & Hein, A. S. in *Exploration of Subsurface Antarctica: Uncovering Past Changes and Modern Processes* (eds Siegert, M. J., Jamieson, S. S. R. & White, D. A.) <https://doi.org/10.1144/SP461.7> (Geological Society, 2017).
30. Farmer, G. L. & Licht, K. J. Generation and fate of glacial sediments in the central Transantarctic Mountains based on radiogenic isotopes and implications for reconstructing past ice dynamics. *Quat. Sci. Rev.* **150**, 98–109 (2016).
31. Goodge, J. W. Geological and tectonic evolution of the Transantarctic Mountains, from ancient craton to recent enigma. *Gondwana Res.* **80**, 50–122 (2020).
32. Licht, K. J. & Palmer, E. F. Erosion and transport by Byrd Glacier, Antarctica during the last glacial maximum. *Quat. Sci. Rev.* **62**, 32–48 (2013).
33. Licht, K. J., Hennessy, A. J. & Welke, B. M. The U-Pb detrital zircon signature of West Antarctic ice stream tills in the Ross embayment, with implications for Last Glacial Maximum ice flow reconstructions. *Antarct. Sci.* **26**, 687–697 (2014).
34. Bader, N. A., Licht, K. J., Kaplan, M. R., Kassab, C. & Winckler, G. East Antarctic ice sheet stability recorded in a high-elevation ice-cored moraine. *Quat. Sci. Rev.* **159**, 88–102 (2017).
35. Kyle, R. A. & Schopf, J. M. in *Antarctic Geoscience* (ed. Craddock, C.) 649–659 (Univ. Wisconsin Press, 1982).
36. Perotti, M., Andreucci, B., Talarico, F., Zattin, M. & Langone, A. Multianalytical provenance analysis of Eastern Ross Sea LGM till sediments (Antarctica): Petrography, geochronology, and thermochronology detrital data. *Geochem. Geophys. Geosyst.* **18**, 2275–2304 (2017).
37. Jordan, T. A., Riley, T. R. & Siddoway, C. S. The geological history and evolution of West Antarctica. *Nat. Rev. Earth Environ.* **1**, 117–133 (2020).
38. Balshaw-Biddle, K. M. *Antarctic Glacial Chronology Reflected in the Oligocene through Pliocene Sedimentary Section in the Ross Sea* PhD Thesis, Rice University (1981).
39. Westerhold, T. et al. An astronomically dated record of Earth's climate and its predictability over the last 66 million years. *Science* **369**, 1383–1387 (2020).
40. Koppes, M. et al. Observed latitudinal variations in erosion as a function of glacier dynamics. *Nature* **526**, 100–103 (2015).
41. Alley, R. B., Cuffey, K. M. & Zetl, L. K. Glacial erosion: status and outlook. *Ann. Glaciol.* **60**, 1–13 (2019).
42. Cox, S. C., Smith Lytle, B. and the GeoMAP team. SCAR GeoMAP dataset. GNS Science, Lower Hutt, New Zealand. Release v.201907 <https://doi.org/10.21420/7SH7-6K05> (2019).
43. Morlighem, M. *MEaSUREs BedMachine Antarctica, Version 1* (Boulder, Colorado USA: NASA National Snow and Ice Data Center Distributed Active Archive Center, 2019; accessed 10 June 2021); <https://doi.org/10.5067/C2GFER6PTOS4>.
44. Morlighem, M. et al. Deep glacial troughs and stabilizing ridges unveiled beneath the margins of the Antarctic ice sheet. *Nat. Geosci.* **13**, 132–137 (2020).
45. Mouginot, J., Scheuchl, B. & Rignot, E. *MEaSUREs Antarctic Boundaries for IPY 2007–2009 from Satellite Radar, Version 2* (Boulder, Colorado USA: NASA National Snow and Ice Data Center Distributed Active Archive Center, 2017; accessed 12 June 2020); <https://doi.org/10.5067/AXE4121732AD>.
46. Rignot, E., Jacobs, S. S., Mouginot, J. & Scheuchl, B. Ice-shelf melting around. *Antarct. Sci.* **341**, 266–270 (2013).
47. Tinto, K. J. et al. Ross Ice Shelf response to climate driven by the tectonic imprint on seafloor bathymetry. *Nat. Geosci.* **12**, 441–449 (2019).
48. Vermeesch, P. Statistical models for point-counting data. *Earth Planet. Sci. Lett.* **501**, 112–118 (2018).
49. Ogg, J. *Geomagnetic Polarity Time Scale. In Geologic Time Scale 2020* (eds Gradstein, F. M. et al.) 159–192 (Elsevier, 2020).
50. Rae, J. W. et al. Atmospheric CO₂ over the past 66 million years from marine archives. *Annu. Rev. Earth Planet. Sci.* **49**, 599–631 (2021).
51. Vermeesch, P. Multi-sample comparison of detrital age distributions. *Chem. Geol.* **341**, 140–146 (2013).

Publisher's note Springer Nature remains neutral with regard to jurisdictional claims in published maps and institutional affiliations.

© The Author(s), under exclusive licence to Springer Nature Limited 2021

IODP Expedition 374

Jeanine Ash²⁵, François Beny⁵, Imogen M. Browne¹³, Giuseppe Cortese¹¹, Laura De Santis¹⁰, Justin P. Dodd²⁴, Oliver M. Esper²⁶, Jenny A. Gales²⁷, David M. Harwood¹⁷, Saki Ishino², Benjamin A. Keisling¹, Sookwan Kim²⁹, Sunghan Kim³⁰, Denise K. Kulhanek^{14,15}, Jan Sverre Laberg³¹, R. Mark Leckie³², Robert M. McKay¹⁶, Julianne Müller³³, Molly O. Patterson³⁴, Brian W. Romans³⁵, Oscar E. Romero³⁶, Francesca Sangiorgi¹⁸, Osamu Seki³⁷, Amelia E. Shevenell¹³, Shiv M. Singh³⁸, Isabela M. Cordeiro de Sousa³⁹, Saiko T. Sugisaki²⁸, Tina van de Flierdt¹, Tim E. van Peer^{3,12}, Whenshen Xiao⁴⁰ & Zifang Xiong⁴¹

²⁵Department of Earth, Environmental and Planetary Sciences, Rice University, Houston, TX, USA. ²⁶Helmholtz Centre for Polar and Marine Research, Alfred Wegener Institute, Bremerhaven, Germany. ²⁷School of Biological & Marine Sciences, Plymouth University, Plymouth, UK. ²⁸Marine Geology Research Group, Geological Survey of Japan, AIST, Tsukuba, Japan. ²⁹Division of Polar-Earth System Sciences, Korea Polar Research Institute, Incheon, Republic of Korea. ³⁰Division of Polar Paleoenvironment, Korea Polar Research Institute, Incheon, Republic of Korea. ³¹Department of Geology, University of Tromsø, Tromsø, Norway. ³²Department of Geosciences, University of Massachusetts, Amherst, Amherst, MA, USA. ³³Marine Geology, Alfred Wegener Institute, Bremerhaven, Germany. ³⁴Department of Geological Sciences and Environmental Studies, Binghamton University, State University of New York, Binghamton, NY, USA. ³⁵Department of Geosciences, Virginia Tech, Blacksburg, VA, USA. ³⁶MARUM, University of Bremen, Bremen, Germany. ³⁷Institute of Low Temperature Science, Hokkaido University, Hokkaido, Japan. ³⁸Polar Biology Lab, National Centre for Polar and Ocean Research (NCPOR) Headland Sada, Vasco-da-Gama, Goa, India. ³⁹Instituto de Geociencias, Universidade de Brasília, Campus Universitário Darcy Ribeiro, Brasília, Brazil. ⁴⁰State Key Laboratory of Marine Geology, Tongji University, Shanghai, China. ⁴¹First Institute of Oceanography, Ministry of Natural Resources, Qingdao, China.

Methods

Neodymium and strontium isotopes

Samples were disaggregated and wet sieved to isolate the <63 µm fraction, which was then dried at 60 °C. This size fraction represents the bulk composition, as samarium and neodymium are incorporated in equal proportions into most rock-forming minerals, meaning grain-size sorting is not likely to impact results^{52,53}. However, the Rb–Sr system is subject to elemental fractionation during weathering and grain-size sorting, which can influence ⁸⁷Sr/⁸⁶Sr ratios (see ‘Provenance Changes within Sequence 2’ section in Supplementary Information). To remove authigenic Fe–Mn oxyhydroxide phases, samples were leached in a mixture of 0.05 M hydroxylamine hydrochloride, 15% acetic acid, and 0.03 M EDTA at a pH of 4⁵⁴. A carbonate removal step was not included due to the very low carbonate content²⁶. Leached sediment was dried, homogenized, and 50-mg aliquots were digested on a hotplate in concentrated HF (2 ml), HClO₄ (0.8 ml) and HNO₃ (1 ml) for three to five days, with a subsequent 6 M HCl step. The Nd was isolated from the sample matrix using a cation exchange resin (AG50W-X8, 200–400 µm mesh) and HCl in increasing molarity, followed by a low molarity HCl Ln-Spec resin procedure (50–100 µm mesh). The sample matrix from the cation exchange step was dried down, taken up in HNO₃, then loaded onto Eichrom Sr Spec resin to wash down the matrix and elute the Sr (ref. ⁵⁵).

Neodymium isotopes were measured in the MAGIC laboratories at Imperial College London on a Nu high resolution multi-collector inductively coupled plasma mass spectrometer (HR MC-ICP-MS). To account for instrumental mass bias, isotope ratios were corrected using an exponential law and a ¹⁴⁶Nd/¹⁴⁴Nd ratio of 0.7219. Although negligible, interference of ¹⁴⁴Sm on ¹⁴⁴Nd was corrected for. Bracketing standards were used to correct measured ¹⁴³Nd/¹⁴⁴Nd ratios to the commonly used JNd-1 value of 0.512115 (ref. ⁵⁶). USGS BCR-2 rock standard was processed alongside all samples and yielded ¹⁴³Nd/¹⁴⁴Nd ratios consistently within error of the published ratio⁵⁷ of 0.512638 ± 0.000015. Full procedural blanks for Nd ranged from 7 to 30 pg ($n = 6$). ¹⁴³Nd/¹⁴⁴Nd ratios are expressed using epsilon notation (ε_{Nd}), which denotes the deviation of a measured ratio from the modern Chondritic Uniform Reservoir (0.512638)⁵⁸ in parts per 10,000.

Sr isotopes were measured in the MAGIC laboratories at Imperial College London on a TIMS (thermal ionization mass spectrometer). 10% of the sample was loaded in 1 µl of 6 M HCl onto degassed tungsten filaments with 1 µl of TaCl₅ activator. The measured ⁸⁷Sr/⁸⁶Sr ratios were corrected for instrumental mass bias using an exponential law and an ⁸⁸Sr/⁸⁶Sr ratio of 8.375. Interference of ⁸⁷Rb was corrected for using an ⁸⁷Rb/⁸⁵Rb ratio of 0.386. Analyses of the NIST 987 standard reference material were completed every four unknowns, yielding a mean of 0.710290 ± 0.000041 (2 s.d., $n = 36$). Samples were corrected to the published value⁵⁷ of 0.710252 ± 0.000013. The relatively poor reproducibility for our NIST 987 runs was due to technical issues, but is still more than sufficient for interpreting sample results, which change in the third to fourth digit. Accuracy of results was confirmed using rock standard USGS BCR-2, processed with every batch of samples, which yielded ⁸⁷Sr/⁸⁶Sr ratios of 0.705010 ± 0.000029 (2 s.d., $n = 18$). This is well within error of the published ratio of 0.705013 ± 0.00010⁵⁷.

Detrital zircon U–Pb dating

The sub-bottom depth midpoints of the nine samples are: A: 220.23, B: 270.03, C: 335.72, D: 373.58, E: 410.82, F: 487.40, G: 546.55, H: 588.00 and I: 642.21 mbsf. To ensure there were enough grains for statistical analysis, the above samples were taken over 40-cm intervals. Samples were disaggregated, dried and sieved at 300 µm. Zircons from the <300 µm fraction were concentrated using standard gravity settling and magnetic separation techniques. Samples were then mounted in resin, polished and analysed using an Agilent 7900 laser ablation inductively coupled plasma mass spectrometer (LA-ICP-MS) with a 25–35 µm pit diameter in the London Geochronology Centre at University

College London. Approximately 150 grains resembling zircons were randomly selected for analysis from each sample. Plešovice zircon⁵⁹ was used as a primary standard to correct for instrumental mass bias and depth-dependent inter-element fractionation. Approximate U and Th concentrations were calculated by comparison with NIST 612 glass⁶⁰.

Data reduction of the time-resolved mass spectrometer data was performed using GLITTER 4.5 (ref. ⁶¹). Ages younger than 1,100 Ma were calculated using the ²⁰⁶Pb/²³⁸U ratio while older grains used the ²⁰⁷Pb/²⁰⁶Pb ratio. Data were filtered to exclude non-zircons based on zirconium concentrations (>10⁶ counts per second) and a –5/+15% discordance threshold was applied. This yielded at least 92 grains per sample, giving a 95% confidence that any age populations comprising more than 7% of the sample will be measured⁶². GJ1 zircon⁶³ was used as a secondary standard to verify accuracy of the data. Repeat analyses using zircons with and without existing ablation pits were made to check sample reproducibility; these agreed within the uncertainties associated with random sampling. Final data were processed and visualized using the R package IsoplotR⁶⁴.

Clast petrography

The gravel fraction (>2 mm) was characterized in continuum along the core between 648.17 and 209.17 mbsf. Clasts exposed in the cut surface of the archive half core were measured, logged and described on the basis of macroscopic features (for example, shape, colour, texture). Logging aimed to identify the distribution and variation of the gravel-size clasts along the core length. Clast logging followed the methods previously applied to the ANDRILL and Cape Roberts Project drill records from the Ross Sea. On the basis of macroscopic features, clasts were grouped into seven main lithological groups: igneous rocks, quartz fragments, dolerites, volcanic rocks, metamorphic rocks, sedimentary rocks and sedimentary intraclasts^{65–68}. Data processing involved counting the occurrence of each lithological group over 10 cm core intervals and summarizing this for each core (Extended Data Fig. 3). The total number of clasts was also summed for each metre interval (Extended Data Fig. 3). To highlight the along-core variation in dolerite and volcanic clasts – two of the most indicative lithologies for provenance constraint – the number of these clasts was divided by the total number of clasts in each core (Extended Data Fig. 3). A total of 73 pebble to cobble-sized clasts were sampled for petrographic analysis, of which the most representative of each lithological group were analysed using standard petrographic methods with polarized light microscopy.

Palynology

Sample processing was performed at Utrecht University, following standard techniques of the Laboratory of Palaeobotany and Palynology. Samples were oven-dried and weighed (~15 g dry weight sediment each). One *Lycopodium clavatum* tablet with a known amount of marker spores was added for quantification of palynomorph abundances⁶⁹.

Samples were treated with 10% HCl and cold 38% HF, then sieved over a 10 µm mesh with occasional mild ultrasonic treatment. To avoid any potential processing-related preservation bias, no oxidation or acetolysis was carried out. The processed residue was transferred to microscope slides using glycerine jelly as a mounting medium, and two slides were analysed per sample at 400 × magnification. Slides were examined for detailed marine palynomorphs (dinoflagellate cysts, acritarchs and other aquatic palynomorphs) and, at screening-level, terrestrial palynomorphs (pollen and spore) at Utrecht University. Subsequent detailed analysis of terrestrial palynomorphs on a sub-set of seven samples was undertaken at GNS Science. Of the 23 palynological samples analysed for dinocysts, two contained <60 dinocysts (Sequence 1; 594.48 mbsf and Sequence 2; 567.75 mbsf) and one was almost barren (yielding only 12 in situ dinocysts, Sequence 3A; 374.9 mbsf). The almost barren sample is excluded from all plots. The two low abundance samples are included in our plots but require careful

interpretation. Samples between 594.48 and 567.75 mbsf and below 594.48 mbsf (cores 65R, 67R, 69R and 71R) were also checked, but yielded few dinocyst specimens. Those present comprised of fragments of mostly reworked dinocysts.

Pollen and spore identification followed taxonomic compilations^{70,71}, augmented by key Antarctic literature^{72–74}. For pollen and spores, scanning continued until an entire cover slide was completed, or a 100 count reached. Results are presented as specimens per gram, and percentage of all terrestrial palynomorphs. Dinocysts were identified based on a taxonomical index⁷⁵ and informally and formally described species in the literature^{76–79}. Dinocyst percentages were calculated based on the total in situ dinocysts counted, excluding reworked specimens. The percentages of other palynomorph groups such as brackish and freshwater algae (*Cymatiosphaera* spp. and *Pediastrum* spp.) and reworked dinocysts were calculated using the total palynomorphs counted (Fig. 2; Extended Data Fig. 2). In situ dinocyst and terrestrial palynomorph absolute abundance (specimens/g dry weight) and the absolute abundance of the other palynomorph groups were calculated by counting the amount of *Lycopodium clavatum* spores encountered, following the equation of Benninghoff⁸⁰.

Protoperidinioid (P) dinocysts are mostly represented by the genera *Brigantedinium*, *Lejeuneacysta* and *Selenopemphix*. Gonyaulacoid (G) dinocysts mostly include *Batiacasphaera* spp., *Operculodinium* spp. and *Spiniferites* spp. Protoperidinioid cyst percentages (heterotrophic % in Extended Data Fig. 2) and percentages of the most common species (*Brigantedinium* spp., *Lejeuneacysta* spp., *Selenopemphix* spp. and *Selenopemphix antarctica*) were calculated to identify productivity trends and/or the presence of sea ice (Supplementary Information). It is likely that P dinocysts are produced by heterotrophic dinoflagellates⁸¹ and, at present, they dominate the assemblages in Antarctic sediments in areas with high nutrients and/or (year-round) sea-ice cover. At present, samples in quasi perennial sea-ice covered areas are dominated by *Selenopemphix antarctica* (~75%), with abundant *Brigantedinium* spp. and rare occurrence of other species^{82–84}. G cysts are generally produced by phototrophic dinoflagellates. *Operculodinium* spp. is the most abundant, has species representatives among the extant cysts and has been selected to represent temperate-warm conditions. At present, it is almost exclusively found in temperate areas of the Southern Ocean north of the Subantarctic Front and never occurs in circum-Antarctic sediments south of the Polar Front⁸². In contrast, it is common to abundant in other Antarctic warm Miocene records^{85,86}. Reworked dinocysts include Eocene and Oligocene taxa (mostly *Vozzhennikovia* spp., but also few *Spinidinium* spp. and *Enneadocysta diktyostila*).

Sediment volume estimate

The volume of sediment comprising Sequence 2 was estimated based on seismic data for the Ross Sea continental shelf²³. The isopach maps were developed by interpolating between available seismic reflection profiles²³, giving a total volume of $175,526 \pm 17,553 \text{ km}^3$. The 10% uncertainty accounts for uncertainty in seismic velocities, which vary from 1,700–2,700 ms⁻¹ at Site U1521 based on tomography and 1,970–2,480 ms⁻¹ based on down-hole measurements. As the provenance data suggest a West Antarctic sediment source for Site U1521 Sequence 2, we assume that all the sediments east of 180° and south of 73° are derived from West Antarctica. This is the vast majority ($123,627 \pm 12,363 \text{ km}^3$) of the sediment across the shelf. Our sediment volume estimate is conservative, as the top of Sequence 2 (surface D-b) has been truncated across much of the continental shelf by RSU4²³. Significant sediment volumes are also likely to be present beyond the edge of the seismic data from the continental rise. Any sediment beneath the modern Ross Ice Shelf is also unaccounted for, although this component is likely to be small.

To translate this sediment volume into an erosion rate, the approach and uncertainty range of Paxman et al.¹⁸ was used to account for porosity and a small biogenic sediment component (Extended Data Table 2). We note that using generic values in our porosity calculation is crude,

with variation in the porosity of these Antarctic sediments likely to be significant,⁸⁷ but nevertheless sufficient for our order-of-magnitude estimate of erosion. It is reasonable to assume the major ice divides have remained in largely the same positions since the Early Miocene, as indicated by various modelling studies using reconstructed topographies^{4,5,16}. The size of the eastern Ross Sea catchment (that is, Ross Sea sector of the WAIS) was therefore assumed to be similar to the modern, with a 20% uncertainty. Some sediment in these units clearly contains reworked material; there are high concentrations of Eocene–Oligocene palynomorphs and diatoms. Although this means our erosion rate is not indicative of pure bedrock incision, it still represents a significant change to the topography and bathymetry of West Antarctica. It is likely that the material removed exceeds our conservative estimate of ~87 m across the catchment. The 317,416-year duration is based on the cyclostratigraphic analyses described in the age model section, with a 20,000-year uncertainty.

IODP Site U1521 age model

The age model for IODP Site U1521 uses magnetostratigraphy, biostratigraphy, cyclostratigraphy, ⁸⁷Sr/⁸⁶Sr dating of macrofossils, and ⁴⁰Ar/³⁹Ar ages of hornblende grains to correlate rock units to the Geomagnetic Polarity Timescale (GPTS)⁴⁹. Key events and tie points are summarized in Extended Data Table 1 and illustrated in Extended Data Figs. 1 and 8. Biostratigraphic constraints include first and last appearance datums of diatoms. The maximum and minimum age range reported for these datums are derived from total and average ranges^{88,89} and hybrid range models derived from Constrained Optimization (CONOP) methods^{89,90}. Hybrid range model ages are used as primary constraints for our age model. This is because they best account for up-section reworking of microfossil datums, which is common in glacial sedimentary environments, while recognizing that major down-section reworking is unlikely (partly because of the rarity of bioturbated intervals). They are marked by base of arrows in Extended Data Fig. 1 and mentioned in the text below. Biostratigraphic datums and magnetic polarity reversals provide tie points to construct lines of correlation (LOC) with the GPTS. The age model presented here includes the interval of West Antarctic sediment provenance (Sequence 2) and is described from the base of the borehole at 650 mbsf to 75 mbsf.

Biostratigraphic constraints through the interval from 650 mbsf to near the top of Sequence 3B (at ~286.1 mbsf) are sparse as the sediments are deeper than the Opal-CT transition and diatom preservation is relatively poor. Our correlation of the four distinct magnetozones R5, N4, R4, and N3 to the GPTS is therefore primarily based on regional correlation of prominent seismic reflectors to other dated drill cores from the Ross Sea shelf, backed up by diatom biostratigraphic constraints. The section from 650 mbsf to 567.95 mbsf at Site U1521 (Sequence 1) is characterized by reversed magnetic polarity but offers no constraints that we can confidently use for correlating this reversed interval to the GPTS. However, robust age constraint for sediments at the base of Sequence 2 can be determined through regional correlation of RSU5 to other sites where chronostratigraphic data are available. RSU5 intersects Site U1521 at 567.95 mbsf (the base of Sequence 2) and is correlated across the Glomar Challenger Basin and tied to DSDP Site 273 at 282 mbsf²³. The LAD of *T. praefraga* is observed at 309 mbsf in DSDP Site 273, which suggests that RSU5 is younger than 17.95 Ma at that site. RSU5 cannot be directly correlated into the western Ross Sea, but a major unconformity (U2) occurs in the AND-2A drill site at 774.94 mbsf, and it is likely that this corresponds with RSU5 based on chronostratigraphy¹¹. Specifically, sediments that directly underlie U2 in AND-2A are characterized by a reversed magnetic polarity and are correlated to Chron C5Er (18.636 to 18.497 Ma) based on constraints that include ⁴⁰Ar/³⁹Ar dates of 18.82 ± 0.15 Ma on pumice clasts within a tuffaceous siltstone at 831.66 mbsf. The age of sediments that overlie U2 at the AND-2A drill site are constrained by the FAD of *T. praefraga* at 771.5 mbsf (<18.46 to 18.58 Ma), and a ⁴⁰Ar/³⁹Ar date of 18.04 ± 0.31 Ma

Article

on pumice clasts within a tuffaceous siltstone at 709.17 mbsf. These observations require correlation of the reversed magnetic polarity zone that characterize the sediments above U2 to Chron C5Dr.2r (18.007 to 17.676 Ma). All evidence presented above shows that between -18.6 and -17.8 Ma, a significant, regionally extensive, erosional event (or series of events) created surface RSU5/U2.

Sediments deposited on top of RSU5 at Site U1521 are characterized by reversed magnetic polarity. Based on the known age of RSU5 at DSDP Site 273 and U2 at AND-2A, we correlate the top of reversed magneto-zone R5 in Site U1521 to Chron C5Dr.2r. This interpretation is consistent with the observation that *T. praefraga* is not present in a diatom-bearing sample at 563 mbsf, despite comprehensive searches for this species in this sample as well as diatom-bearing samples higher in Sequence 2. As *T. praefraga* is a small and compact diatom not prone to fragmentation that is likely to be preserved in the observed diatom assemblages, we are confident this absence is not a result of poor preservation below the Opal-CT transition. *T. praefraga* is a common species in upper Oligocene and lower Miocene sediments recovered from several sites across the Ross Sea, including Cape Roberts Project-2/2A, DSDP Site 273, and AND-2A^{11,91,92}. The total reported CONOP model based age range for the LAD of *T. praefraga* is 17.95 to 16.82 Ma and the hybrid model range is 17.95 to 17.36 Ma^{88–90}. Consequently, we view the absence of *T. praefraga* as strong evidence that the sediments above 563 mbsf at Site U1521 are younger than 17.95 Ma.

We then correlate the magnetic polarity reversal (MPR) R5/N5 between 526.8 and 524 mbsf to C5Dr.1n/C5Dr.2r (17.676 Ma), the MPR N4/R4 between 517.2 and 515.1 mbsf to C5Dr.1r/C5Dr.1n (17.634 Ma), and the MPR R4/N3 between 400.5 and 397.2 mbsf to C5Dn/C5Dr.1r (17.466 Ma). We extend a line of correlation from this MPR to the top of Sequence 2, where it intersects with seismic surface D-b²³. The correlation presented here by interpolating through these MPRs indicates sediments in Sequence 2 span the time interval from -17.7–17.4 Ma. The occurrence of the diatom taxon *Thalassiosira* sp. cf. *T. bukryi* at 450.52 mbsf supports this correlation as the range reported for this taxon at ODP Site 744 is 17.7–17.4 Ma^{89,93}.

To refine the likely sedimentation rate and timespan of Sequence 2, a cyclostratigraphic analysis was conducted on clast abundance data (Extended Data Fig. 3) spanning 568 to 380 mbsf. These data were analysed using TimeOpt⁹⁴, which is a statistical optimization method for astronomical time scale construction and astrochronologic testing, executed by the *astrochron* package in R (function ‘timeOpt’)⁹⁵. Given a range of plausible sedimentation rates and a series of specified astronomical periodicities (for precession, obliquity and eccentricity), TimeOpt identifies the age model that results in a time-series that best aligns with the predictions of Milankovitch theory. Specifically, two diagnostic attributes of the astronomical hypothesis are evaluated: the hierarchy of cyclic frequencies expected of Milankovitch Cycles, r^2_{spectral} , and the match between eccentricity cycles and the precession-band envelope, r^2_{envelope} ^{94,96}. These two values (r^2_{power} and r^2_{envelope}) are multiplied to produce an r^2_{opt} value, which provides insight into the strength of a hypothesized astronomical signal at each evaluated sedimentation rate.

Assuming plausible average sedimentation rates between 40 cm kyr⁻¹ and 65 cm kyr⁻¹, TimeOpt yields an optimal sedimentation rate of 59.2 cm kyr⁻¹ for Sequence 2, with an r^2_{opt} of 0.396. To assess the statistical significance of the result, a Monte Carlo astrochronologic test is conducted to evaluate the null hypothesis that the observed variability in clast abundance arises entirely by stochastic processes, rather than astronomical forcing. The Monte Carlo simulations are generated using the function ‘timeOptSim’, which creates a large number of similar time-series of stochastic (‘red’) noise, to assess the probability that such data sets can produce an r^2_{opt} value comparable to the one generated by the clast abundance data^{94,96}. This analysis yields a p value of 0.005, indicating that the null hypothesis (that is, the data are generated from a stochastic ‘red noise’ process; specifically an AR1 process) can be

rejected with a high degree of confidence. Given that the astrochronologically estimated sedimentation rate is derived independently from the paleomagnetic data, their consistency is remarkable and provides strong evidence in support of an estimated duration of ~317 kyr for Sequence 2 (Extended Data Fig. 1)²⁶.

Although the ‘floating’ TimeOpt-derived astronomical timescale preserves information about elapsed time, it must be separately anchored to a specific numerical age. To do so, we use the ‘slideCor’ function in the *astrochron* package⁹⁵; this is an automated approach to find the optimal anchoring of the floating TimeOpt-derived timescale to the theoretical astronomical solution of Laskar et al.⁹⁷. Specifically, we have applied a Taner bandpass filter⁹⁸, isolating the periods between 60 ka and 27 ka for both the obliquity component of the astronomical solution⁹⁷, and for the TimeOpt-derived floating astrochronology. The optimal match between the astronomical solution and floating astrochronology is identified using the squared Pearson correlation coefficient.

Independent biostratigraphic and magnetostratigraphic constraints mean we can restrict our ‘slideCor’ assessment to a feasible ~800 ka interval; our lower limit (17.950 Ma) is based on the absence of *T. praefraga* and the correlations of RSU5 described above, and our upper limit is based on the C5Cr/C5Dn MPR (17.154 Ma). Since the precise relationship between clast abundance and astronomical forcing is not known with certainty, any time-anchor for the astronomically calibrated section should be treated as having an uncertainty of at least a full obliquity cycle (~41 ka). Application of the slideCor function identifies two plausible regions of the astronomical solution for anchoring the Sequence 2 clast abundance data. The optimal match ($r^2 = 0.8497$) results in an astronomically calibrated section ranging from 17.601 Ma to 17.918 Ma (± 0.02 Ma). This would indicate that the interval is ~140–220 kyr older than the age range suggested by the paleomagnetic interpretation, giving a very poor match with the measured polarities. However, a slightly less optimal match ($r^2 = 0.7704$) anchors the section to span 17.398 Ma to 17.715 Ma (± 0.02 Ma), which places it within ~40 kyr of the paleomagnetic interpretation. This agreement of geochronological frameworks derived from paleomagnetism and astrochronology, which are broadly independent, provides strong support for the age model presented here.

Uncertainties in the magnetostratigraphic age model, most notably for Subchrons C5Dr.1n and C5Dr.1r and Chron C5Dn, may account for some of the slight disagreement with the astrochronological approach described above. The available astronomically tuned durations of these (sub-)chrons agree within 10%^{99,100}. The small discrepancies in duration of (sub-)chrons originate from the astronomical tuning approach (carbon and oxygen isotopes tuned to eccentricity, tilt and precession at Site 1090 (ref. ⁹⁹) and carbonate content to eccentricity only at Site U1336 (ref. ¹⁰⁰), as well as physical and palaeomagnetic recording processes such as bioturbation and the palaeomagnetic lock-in depth^{101,102}. Paleomagnetic measurement methods are discussed in detail in the cruise report²⁶.

We suggest 17.95–17.40 Ma as the absolute uncertainty of the timing of Sequence 2 deposition, based on the absence of *T. praefraga* (17.95 Ma) and occurrence of MPR C5Dn/C5Dr.1r (17.466 Ma) near the top of Sequence 2. However, more precise constraint on the duration of Sequence 2 deposition can be achieved based on the remarkable agreement of sedimentation rates based on the astronomical analysis of clast data and interpolation through magnetostratigraphic tie points, which suggest deposition occurred over ~317 kyr. Combined with the close correlation between our astrochronological analyses and the timing of MPRs, we suggest a more precise interval for the deposition of Sequence 2, spanning $-17.72\text{--}17.40 \pm 0.02$ Ma. The ~20 kyr error represents uncertainty in the phase relationship between clast abundance and obliquity forcing. This range coincides closely with many independent records indicating ice-sheet growth, including a sea-level lowstand recorded on the New Jersey continental margin (~17.8–17.46 Ma)¹, evidence for

ice sheet growth in the AND-2A drill core sediments (-17.8 – 17.4 Ma)¹¹ and a peak in obliquity sensitivity (-17.8 – 17.5 Ma)¹⁵ (Fig. 2).

The age of Sequence 3A and 3B (324.20–209.17 mbsf), bracketed by seismic surface D-b and regional unconformity RSU4a, is difficult to tightly constrain. Diatom preservation increases significantly in a sample at 286.1 mbsf at the base of Sequence 4A and the FADs of *Nitzschia* sp., *17 Schrader*, *Synedropsis cheethamii* and *Denticulopsis maccollumii* suggest sediments below this stratigraphic level are older than 17 Ma. The LAD of *F. maleinterpretaria* in this sample provides a minimum age constraint and suggests that the sediments below 286.1 Ma must be older than 16.41 Ma. These constraints require that the sediments between 344.6 and 286.3 mbsf, characterized by reversed polarity, correlate with either the Subchron C5Cn.2r or the base of Chron C5Cr. Correlation to the base of Chron C5Cr is our favoured option as this would indicate that the interval of time missing across seismic surface D-b is relatively short, whereas regional unconformity RSU4a at the top of this unit records a hiatus of longer duration. The alternative interpretation is shown with a dashed line in Extended Data Fig. 1.

We constrain the slope of the LOC through Sequence 3B based on the sedimentation rate indicated for the diatom-bearing Sequence 4B as the sediments are similar, although affected by diagenesis in Sequence 3B. The sedimentation rate in Sequence 3A is assumed to be comparable to the Sequence 2 diamicts. We also acknowledge that the actual first appearance of the diatom taxa identified in the sample at 286.1 mbsf may have originally been deeper, but their presence has since been obscured by diagenesis. This would require that the LOC sit to the left (younger) of its current position. Therefore, we include an error box (orange box in Extended Data Fig. 1) in our age model to show that the LOC could occur anywhere within this area depending on the amount of time missing across D-b and the sedimentation rate during deposition. We are confident that the MPR between 400.5 and 397.2 mbsf (N3/R3) is CSDn/C5Dr.1r (17.466 Ma) based on constraints above and below this interval outlined above and place our LOC through the reversal. This LOC requires a time gap of ~180 kyr across regional seismic surface D-b²³ that separates Sequences 2 and 3.

The relatively thin interval of reversed polarity within Chron CSDn (at ~380 mbsf) is not identified in the current version of the GPTS (Extended Data Fig. 8), but a similar short-duration reversed polarity event roughly halfway through Chron CSDn is recorded in the AND-2A magnetostratigraphic record¹¹. Taking the palaeomagnetic uncertainties of ice-proximal sediments into account, we hypothesize that this rarely recorded reversed polarity event could be a genuine feature of the geomagnetic field that has not been detected in marine sediments due to signal smoothing at low sedimentation rates¹⁰³.

The age of sediments above RSU4a are very well constrained by diatom data, $^{87}\text{Sr}/^{86}\text{Sr}$ ages and magnetostratigraphy. The LAD of *F. maleinterpretaria* indicates that the sediments above 286.1 mbsf must be younger than 16.41 Ma. An $^{87}\text{Sr}/^{86}\text{Sr}$ date on shell fragments at 272.65 mbsf indicates the interval with reversed polarity containing the fragments correlates with Subchron C5Cn.1r (16.351 to 16.261 Ma). This correlation means that the hybrid age model underestimates the maximum age of the FAD of *Nitzschia grossepunctata*, which occurs at 286.1 mbsf, and suggests the age indicated by the total range model age for this datum (16.23 Ma) is more likely. Together, these data indicate that the base of Sequence 4A dates to less than ~16.351 Ma. We correlate the MPR (R3/N2) between 209 and 205 mbsf to C5Cn.1n/C5Cn.1r (16.261 Ma). The sequence of well-dated shells through Sequence 4B allows us to correlate the sediments between 209 and 106.3 mbsf that are characterized by normal polarity with Subchron C5Cn.1n (16.261 to 15.994 Ma) and the MPR between 106.3 and 105.5 to C5Br/C5Cn.1n (15.994 Ma). The FADs of *Denticulopsis lauta*, *Actinocyclus ingens*, *Denticulopsis hyalina* and *Denticulopsis simonsenii* at 84.99 mbsf indicate a major hiatus at this depth spanning from ~15.83 Ma to at least 14.48 Ma. This stratigraphic horizon correlates with RSU4, a major regional unconformity²³.

Sediment provenance interpretations

To interpret the provenance data from IODP Site U1521, they must be placed in a regional context. In the Supplementary Information, we therefore present a short geological summary of the Ross Sea sector^{31,37,104–170}, including a compilation of published zircon U–Pb data^{33,105–129}. We also include a more detailed discussion of our hornblende $^{40}\text{Ar}/^{39}\text{Ar}$ ^{136,154,171–175}, clast petrography, neodymium and strontium isotope^{176–182}, clay mineralogy^{158,183–188}, and palynology^{35,72,78,84,189–192} data sets. Additional insights into the sediment provenance of Sequences 1, 2 and 3A are also explored^{23,33,38,184,193–199}. A compilation of literature neodymium and strontium isotope data (visualized in Extended Data Figs. 4 and 5) is provided in Supplementary Table 1.

Data availability

The data sets generated as part of this study are available in the British Geological Survey National Geoscience Data Centre. Data sets include Nd and Sr isotope data (<https://doi.org/10.5285/3a646c8a-8422-4079-a928-a159532439eb>), zircon U–Pb dates (<https://doi.org/10.5285/cfadfc931-0804-484c-a9d0-96254239c421>), clast counts (<https://doi.org/10.5285/b043471f-22e5-40e4-b274-1c875316d725>), clay mineralogy data (<https://doi.org/10.5285/b3cb3574-49b0-44c8-a934-3da88ca4ef93>), hornblende $^{40}\text{Ar}/^{39}\text{Ar}$ dates (<https://doi.org/10.5285/926cad28-669f-4703-8a5b-5e7e843a4ee1>) and palynological counts (<https://doi.org/10.5285/adea0809-5fe5-4fb5-9f3e-9d774534d26d>). Source data are provided with this paper.

52. Goldstein, S. L. & Hemming, S. R. in *Treatise on Geochemistry* (eds Holland, H. D. & Turekian, K. K.) 453–489 (Pergamon, 2003).
53. Garçon, M., Chauvel, C., France-Lanord, C., Huyghe, P. & Lavé, J. Continental sedimentary processes decouple Nd and Hf isotopes. *Geochim. Cosmochim. Acta* **121**, 177–195 (2013).
54. Gutjahr, M. et al. Reliable extraction of a deepwater trace metal isotope signal from Fe–Mn oxyhydroxide coatings of marine sediments. *Chem. Geol.* **242**, 351–370 (2007).
55. Simões Pereira, P. et al. Geochemical fingerprints of glacially eroded bedrock from West Antarctica: D–eolian thermochronology, radiogenic isotope systematics and trace element geochemistry in Late Holocene glacial-marine sediments. *Earth Sci. Rev.* **182**, 204–232 (2018).
56. Tanaka, T. et al. JNdI-1: a neodymium isotopic reference in consistency with LaJolla neodymium. *Chem. Geol.* **168**, 279–281 (2000).
57. Weis, D. et al. High-precision isotopic characterization of USGS reference materials by TIMS and MC-ICP-MS. *Geochim. Geophys. Geosyst.* **7**, Q08006 (2006).
58. Jacobsen, S. B. & Wasserburg, G. J. Sm–Nd isotopic evolution of chondrites. *Earth Planet. Sci. Lett.* **50**, 139–155 (1980).
59. Sláma, J. et al. Plešovice zircon—a new natural reference material for UPb and Hf isotopic microanalysis. *Chem. Geol.* **249**, 1–35 (2008).
60. Pearce, N. J. et al. A compilation of new and published major and trace element data for NIST SRM 610 and NIST SRM 612 glass reference materials. *Geostand. Newsl.* **21**, 115–144 (1997).
61. Griffin, W. L. in *Laser Ablation ICP-MS in the Earth Sciences: Current Practices and Outstanding Issues* (ed. Sylvester, P.) 308–311 (Mineralogical Association of Canada, 2008).
62. Vermeesch, P. How many grains are needed for a provenance study? *Earth Planet. Sci. Lett.* **224**, 441–451 (2004).
63. Jackson, S. E., Pearson, N. J., Griffin, W. L. & Belousova, E. A. The application of laser ablation-inductively coupled plasma-mass spectrometry to *in situ* U–Pb zircon geochronology. *Chem. Geol.* **211**, 47–69 (2004).
64. Vermeesch, P. & Isoplot, R. A free and open toolbox for geochronology. *Geoscience Frontiers* **9**, 1479–1493 (2018).
65. Talarico, F. & Sandroni, S. Petrography, mineral chemistry and provenance of basement clasts in the CRP-3 drillcore (Victoria Land Basin, Antarctica). *Terra Antarct.* **5**, 601–610 (1998).
66. Talarico, F. & Sandroni, S. Provenance signature of the Antarctic Ice Sheets in the Ross Embayment during the Late Miocene to Early Pliocene: the ANDRILL AND-1B core record. *Global Planet. Change* **69**, 103–123 (2009).
67. Talarico, F., Sandroni, S., Fielding, C. R. & Atkins, C. Variability, petrography and provenance of basement clasts from CRP-2/2A drillcore (Victoria Land Basin, Ross Sea, Antarctica). *Terra Antarct.* **7**, 529–544 (2000).
68. Sandroni, S. & Talarico, F. M. Petrography and provenance of basement clasts and clast variability in CRP-3 drillcore (Victoria Land Basin, Antarctica). *Terra Antarct.* **8**, 449–467 (2001).
69. Wood, G. D., Gabriel, A. M. & Lawson, J. C. in *Palynology: Principles and Applications* (eds Janssens, J. & McGregor, D. C.) 29–50 (American Association of Stratigraphic Palynologists Foundation, 1996).
70. Raine, J. I., Mildenhall, D. C. & Kennedy, E. M. *New Zealand Fossil Spores and Pollen: An Illustrated Catalogue* (GNS Science Miscellaneous Series No. 4, 4th edition, 2011); <http://data.gns.cri.nz/sporepollen/index.htm>

Article

71. Prebble, J. G. Descriptions and occurrences of pollen and spores from New Zealand Cenozoic sediments. *GNS Science Internal Report* **2016**, 137 (2016).
72. Askin, R. A. in *Palaeobiology and Palaeoenvironments of Eocene Rocks, McMurdo Sound, East Antarctic Antarctic Research Series v76* (eds Stilwel, J. D. & Feldman, R. M.) 161–181 (American Geophysical Union, 2000).
73. Askin, R. A. & Raine, J. I. Oligocene and Early Miocene terrestrial palynology of the Cape Roberts Drillhole CRP-2/2A, Victoria Land Basin, Antarctica. *Terra Antarct.* **7**, 493–501 (2000).
74. Truswell, E. M. Recycled Cretaceous and Tertiary pollen and spores in Antarctic marine sediments: a catalogue. *Palaeontographica Abt. B Paläophytol.* **186**, 121–174 (1983).
75. Fensome, R. A. & Williams, G. L. *The Lentin and Williams Index of Fossil Dinoflagellates* (American Association of Stratigraphic Palynologists Foundation Contribution Series 42, 2004).
76. Hannah, M. J., Wilson, G. J. & Wrenn, J. H. Oligocene and miocene marine palynomorphs from CRP-2/2A, Victoria Land Basin, Antarctica. *Terra Antarct.* **7**, 503–511 (2000).
77. Hannah, M. J. The palynology of ODP site 1165, Prydz Bay, East Antarctica: a record of Miocene glacial advance and retreat. *Palaeogeogr. Palaeoclimatol. Palaeoecol.* **231**, 120–133 (2006).
78. Clowes, C. D., Hannah, M. J., Wilson, G. J. & Wrenn, J. H. Marine palynostigraphy of the Cape Roberts Drill-holes, Victoria Land Basin, Antarctica, with descriptions of six new species of organic-walled dinoflagellate cyst. *Mar. Micropaleontol.* **126**, 65–84 (2016).
79. Bijl, P. et al. Stratigraphic calibration of Oligocene–Miocene organic-walled dinoflagellate cysts from offshore Wilkes Land, East Antarctica, and a zonation proposal. *J. Micropalaeontol.* **37**, 105–138 (2018).
80. Benninghoff, W. S. Calculation of pollen and spores density in sediments by addition of exotic pollen in known quantities. *Pollen Spores* **6**, 332–333 (1962).
81. Harland, R. & Pudsey, C. J. Dinoflagellate cysts from sediment traps deployed in the Bellingshausen, Weddell and Scotia seas, Antarctica. *Mar. Micropaleontol.* **37**, 77–99 (1999).
82. Prebble, J. G. et al. An expanded modern dinoflagellate cyst dataset for the Southwest Pacific and Southern Hemisphere with environmental associations. *Mar. Micropaleontol.* **101**, 33–48 (2013).
83. Hartman, J. D., Bijl, P. K. & Sangiorgi, F. A review of the ecological affinities of marine organic microfossils from a Holocene record offshore of Adélie Land (East Antarctica). *J. Micropalaeontol.* **37**, 445–497 (2018).
84. Zonneveld, K. A. et al. Atlas of modern dinoflagellate cyst distribution based on 2405 data points. *Rev. Palaeobot. Palynol.* **191**, 1–197 (2013).
85. Warny, S. et al. Palynomorphs from a sediment core reveal a sudden remarkably warm Antarctica during the middle Miocene. *Geology* **37**, 955–958 (2009).
86. Sangiorgi, F. et al. Southern Ocean warming and Wilkes Land ice sheet retreat during the mid-Miocene. *Nat. Commun.* **9**, 317 (2018).
87. Niessen, F., Gebhardt, A. C., Kuhn, G., Magens, D. & Monien, D. Porosity and density of the AND-1B sediment core, McMurdo Sound region, Antarctica: Field consolidation enhanced by grounded ice. *Geosphere* **9**, 489–509 (2013).
88. Cody, R. D., Levy, R. H., Harwood, D. M. & Sadler, P. M. Thinking outside the zone: high-resolution quantitative diatom biochronology for the Antarctic Neogene. *Palaeogeogr. Palaeoclimatol. Palaeoecol.* **260**, 92–121 (2008).
89. Florindo, F. et al. Paleomagnetism and biostratigraphy of sediments from Southern Ocean ODP Site 744 (southern Kerguelen Plateau): implications for early-to-middle Miocene climate in Antarctica. *Global Planet. Change* **110**, 434–454 (2013).
90. Crampton, J. S. et al. Southern Ocean phytoplankton turnover in response to stepwise Antarctic cooling over the past 15 million years. *Proc. Natl Acad. Sci. USA* **113**, 6868–6873 (2016).
91. Scherer, R., Bohaty, S. M. & Harwood, D. M. Oligocene and lower Miocene siliceous microfossil biostratigraphy of Cape Roberts Project Core CRP-2/2A, Victoria Land Basin, Antarctica. *Terra Antarct.* **7**, 417–442 (2000).
92. Taviani, M. et al. Palaeontological characterisation and analysis of the AND-2A core, ANDRILL Southern McMurdo Sound Project, Antarctica. *Terra Antarct.* **15**, 113–146 (2008).
93. Farmer, R. K. *The Application of Biostratigraphy and Paleoecology at Southern Ocean Drill Sites to Resolve Early to Middle Miocene Paleoclimatic Events* MS thesis, Univ. Nebraska-Lincoln (2011).
94. Meyers, S. R. The evaluation of eccentricity-related amplitude modulation and bundling in paleoclimate data: An inverse approach for astrochronologic testing and time scale optimization. *Paleoceanography* **30**, 1625–1640 (2015).
95. Meyers, S. R. Astrochron: An R Package for Astrochronology (2014); <http://cran.rproject.org/package=astrochron>
96. Meyers, S. R. Cyclostratigraphy and the problem of astrochronologic testing. *Earth Sci. Rev.* **190**, 190–223 (2019).
97. Laskar, J. et al. A long-term numerical solution for the insolation quantities of the Earth. *Astron. Astrophys.* **428**, 261–285 (2004).
98. Taner, M. T. *Attributes Revised. Technical Report* (Rock Solid Images, 1992).
99. Billups, et al. Astronomic calibration of the late Oligocene through early Miocene geomagnetic polarity time scale. *Earth Planet. Sci. Lett.* **224**, 33–44 (2004).
100. Kochhann, K. G. et al. Eccentricity pacing of eastern equatorial Pacific carbonate dissolution cycles during the Miocene Climatic Optimum. *Paleoceanography* **31**, 1–17 (2016).
101. Suganuma, Y. et al. ^{10}Be evidence for delayed acquisition of remanent magnetization in marine sediments: Implication for a new age for the Matuyama–Brunhes boundary. *Earth Planet. Sci. Lett.* **296**, 443–450 (2010).
102. Suganuma, Y. et al. Post-depositional remanent magnetization lock-in for marine sediments deduced from ^{10}Be and paleomagnetic records through the Matuyama–Brunhes boundary. *Earth Planet. Sci. Lett.* **311**, 39–52 (2011).
103. Roberts, A. P. & Winklhofer, M. Why are geomagnetic excursions not always recorded in sediments? Constraints from post-depositional remanent magnetization lock-in modelling. *Earth Planet. Sci. Lett.* **227**, 345–359 (2004).
104. Boger, S. D. Antarctica—before and after Gondwana. *Gondwana Res.* **19**, 335–371 (2011).
105. Siddoway, C. S. in *Antarctica: A Keystone in a Changing World* (eds Cooper, A., Raymond, C. and the 10th ISAES Editorial Team) 91–114 (The National Academic Press, USA, 2008).
106. Mukasa, S. B. & Dalziel, I. W. Marie Byrd Land, West Antarctica: Evolution of Gondwana's Pacific margin constrained by zircon U-Pb geochronology and feldspar common-Pb isotopic compositions. *Geol. Soc. Am. Bull.* **112**, 611–627 (2000).
107. Weaver, S. D., Adams, C. J., Pankhurst, R. J. & Gibson, I. L. Granites of Edward VII Peninsula, Marie Byrd Land: anorogenic magmatism related to Antarctic-New Zealand rifting. *Earth Environ. Sci. Trans. R. Soc. Edinb.* **83**, 281–290 (1992).
108. Korhonen, F. J., Saito, S., Brown, M., Siddoway, C. S. & Day, J. M. D. Multiple generations of granite in the Fosdick Mountains, Marie Byrd Land, West Antarctica: implications for polyphase intracrustal differentiation in a continental margin setting. *J. Petrol.* **51**, 627–670 (2010).
109. Craddock, J. et al. Precise U-Pb zircon ages and geochemistry of Jurassic granites, Ellsworth-Whitmore terrane, central Antarctica. *Geol. Soc. Am. Bull.* **129**, 118–136 (2017).
110. Pankhurst, R. J., Weaver, S. D., Bradshaw, J. D., Storey, B. C. & Ireland, T. R. Geochronology and geochemistry of pre-Jurassic superterranes in Marie Byrd Land, Antarctica. *J. Geophys. Res. Solid Earth* **103**, 2529–2547 (1998).
111. Flowerdew, M. J. et al. Combined U-Pb geochronology and Hf isotope geochemistry of detrital zircons from early Paleozoic sedimentary rocks, Ellsworth-Whitmore Mountains block, Antarctica. *Geol. Soc. Am. Bull.* **119**, 275–288 (2007).
112. Elliot, D. H. & Fanning, C. M. Detrital zircons from upper Permian and lower Triassic Victoria Group sandstones, Shackleton Glacier region, Antarctica: evidence for multiple sources along the Gondwana plate margin. *Gondwana Res.* **13**, 259–274 (2008).
113. Elliot, D. H., Fanning, C. M. & Hulett, S. R. Age provinces in the Antarctic craton: Evidence from detrital zircons in Permian strata from the Beardmore Glacier region, Antarctica. *Gondwana Res.* **28**, 152–164 (2015).
114. Goodge, J. W., Williams, I. S. & Myrow, P. Provenance of Neoproterozoic and lower Paleozoic siliciclastic rocks of the central Ross orogen, Antarctica: Detrital record of rift-, passive-, and active-margin sedimentation. *Geol. Soc. Am. Bull.* **116**, 1253–1279 (2004).
115. Paulsen, T. S. et al. Detrital mineral ages from the Ross Supergroup, Antarctica: Implications for the Queen Maud terrane and outboard sediment provenance on the Gondwana margin. *Gondwana Res.* **27**, 377–391 (2015).
116. Paulsen, T. S. et al. Correlation and Late-Stage Deformation of Liv Group Volcanics in the Ross-Delamerian Orogen, Antarctica, from New U-Pb Ages. *J. Geol.* **126**, 307–323 (2018).
117. Goodge, J. W., Fanning, C. M., Norman, M. D. & Bennett, V. C. Temporal, isotopic and spatial relations of early Paleozoic Gondwana-margin arc magmatism, central Transantarctic Mountains, Antarctica. *J. Petrol.* **53**, 2027–2065 (2012).
118. Paulsen, T. S. et al. Age and significance of 'outboard' high-grade metamorphics and intrusives of the Ross orogen, Antarctica. *Gondwana Res.* **24**, 349–358 (2013).
119. Rowell, A. J. et al. An active Neoproterozoic margin: evidence from the Skelton Glacier area, Transantarctic Mountains. *J. Geol. Soc. Lond.* **150**, 677–682 (1993).
120. Encarnación, J. & Grunow, A. Changing magmatic and tectonic styles along the paleo-Pacific margin of Gondwana and the onset of early Paleozoic magmatism in Antarctica. *Tectonics* **15**, 1325–1341 (1996).
121. Goodge, J. W., Hansen, V. L., Peacock, S. M., Smith, B. K. & Walker, N. W. Kinematic evolution of the Miller Range shear zone, central Transantarctic Mountains, Antarctica, and implications for Neoproterozoic to early Paleozoic tectonics of the East Antarctic margin of Gondwana. *Tectonics* **12**, 1460–1478 (1993).
122. Van Schmus, W. R., McKenna, L. W., Gonzales, D. A., Fetter, A. H. & Rowell, A. J. U-Pb geochronology of parts of the Pensacola, Thiel, and Queen Maud Mountains, Antarctica. In *The Antarctic Region: Geological Evolution and Processes* (ed. Ricci, C. A.) 187–200 (Terra Antarctica Publication, 1995).
123. Stump, E. *The Ross Orogen of the Transantarctic Mountains* (Cambridge Univ. Press, 1995).
124. Martin, A. P., Price, R. C., Cooper, A. F. & McCammon, C. A. Petrogenesis of the rifted southern Victoria Land lithospheric mantle, Antarctica, inferred from petrography, geochemistry, thermobarometry and oxybarometry of peridotite and pyroxenite xenoliths from the Mount Morning eruptive centre. *J. Petrol.* **56**, 193–226 (2015).
125. Goodge, J. W., Myrow, P., Williams, I. S. & Bowring, S. A. Age and provenance of the Beardmore Group, Antarctica: constraints on Rodinia supercontinent breakup. *J. Geol.* **110**, 393–406 (2002).
126. Stump, E., Gehrels, G., Talarico, F. M. & Carosi, R. Constraints from detrital zircon geochronology on the early deformation of the Ross orogen, Transantarctic Mountains, Antarctica. In *Antarctica: A Keystone in a Changing World – Online Proceedings of the 10th ISAES* (eds Cooper, A. K. et al.) Extended Abstract 166 (USGS Open-File Report 2007-1047, 2007).
127. Cooper, A. F., Maas, R., Scott, J. M. & Barber, A. J. Dating of volcanism and sedimentation in the Skelton Group, Transantarctic Mountains: implications for the Rodinia-Gondwana transition in southern Victoria Land, Antarctica. *Geol. Soc. Am. Bull.* **123**, 681–702 (2011).
128. Goodge, J. W., Fanning, C. M. & Bennett, V. C. U-Pb evidence of ~1.7 Ga crustal tectonism during the Nimrod Orogeny in the Transantarctic Mountains, Antarctica: implications for Proterozoic plate reconstructions. *Precambr. Res.* **112**, 261–288 (2001).
129. Goodge, J. W. & Fanning, C. M. Mesoproterozoic and Paleoproterozoic history of the Nimrod Complex, central Transantarctic Mountains, Antarctica: stratigraphic revisions and relation to the Mawson Continent in East Gondwana. *Precambr. Res.* **285**, 242–271 (2016).
130. Veevers, J. J. & Saeed, A. Age and composition of Antarctic bedrock reflected by detrital zircons, erratics, and recycled microfossils in the Prydz Bay–Wilkes Land–Ross Sea–Marie Byrd Land sector (70–240 E). *Gondwana Res.* **20**, 710–738 (2011).
131. Goodge, J. W. & Fanning, C. M. 2.5 by of punctuated Earth history as recorded in a single rock. *Geology* **27**, 1007–1010 (1999).
132. Grindley, G. W., McGregor, V. R. & Walcott, R. I. In *Antarctic Geology: Proceedings of the First International Symposium on Antarctic Geology* (ed. Adie, R. J.) 206–219 (North Holland, 1964).

133. Laird, M. G. in *The Geology of Antarctica* (ed Tingey R. J.) 74–119 (Oxford Univ. Press, 1991).
134. Goodge, J. W. & Finn, C. A. Glimpses of East Antarctica: Aeromagnetic and satellite magnetic view from the central Transantarctic Mountains of East Antarctica. *J. Geophys. Res. Solid Earth* <https://doi.org/10.1029/2009JB006890> (2010).
135. Goodge, J. W. & Fanning, C. M. Composition and age of the East Antarctic Shield in eastern Wilkes Land determined by proxy from Oligocene-Pleistocene glaciomarine sediment and Beacon Supergroup sandstones, Antarctica. *Geol. Soc. Am. Bull.* **122**, 1135–1159 (2010).
136. Gunn, B. M. & Warren, G. Geology of Victoria Land between the Mawson and Mulock Glaciers, Antarctica. *New Zea. Geol. Bull.* **71**, 157 (1962).
137. Encarnación, J., Rowell, A. J. & Grunow, A. M. A U-Pb age for the Cambrian Taylor Formation, Antarctica: Implications for the Cambrian time scale. *J. Geol.* **107**, 497–504 (1999).
138. Wareham, C. D., Stump, E., Storey, B. C., Millar, I. L. & Riley, T. R. Petrogenesis of the Cambrian Liv Group. A bimodal volcanic rock suite from the Ross orogen, Transantarctic Mountains. *Geol. Soc. Am. Bull.* **113**, 360–372 (2001).
139. Elliot, D. H., Larsen, D., Fanning, C. M., Fleming, T. H. & Vervoort, J. D. The Lower Jurassic Hanson Formation of the Transantarctic Mountains: implications for the Antarctic sector of the Gondwana plate margin. *Geol. Mag.* **154**, 777–803 (2016).
140. Elliot, D. H., Fanning, C. M., Isbell, J. L. & Hulett, S. R. W. The Permo-Triassic Gondwana sequence, central Transantarctic Mountains, Antarctica: Zircon geochronology, provenance, and basin evolution. *Geosphere* **13**, 155–178 (2017).
141. Elsner, M., Schöner, R., Gerdes, A. & Gaupp, R. Reconstruction of the early Mesozoic plate margin of Gondwana by U-Pb ages of detrital zircons from northern Victoria Land, Antarctica. *Geol. Soc. Lond. Spec. Publ.* **383**, 211–232 (2013).
142. Paulsen, T., Deering, C., Śliwiński, J., Bachmann, O. & Guillong, M. New detrital zircon age and trace element evidence for 1450 Ma igneous zircon sources in East Antarctica. *Precambr. Res.* **300**, 53–58 (2017).
143. Zurli, L. et al. Detrital zircons from Late Paleozoic Ice Age sequences in Victoria Land (Antarctica): New constraints on the glaciation of southern Gondwana. *Geol. Soc. Am. Bull.* (2021).
144. Welke, B. et al. Applications of detrital geochronology and thermochronology from glacial deposits to the Paleozoic and Mesozoic thermal history of the Ross Embayment, Antarctica. *Geochem. Geophys. Geosyst.* **17**, 2762–2780 (2016).
145. Vogel, M. B., Ireland, T. R. & Weaver, S. D. The multistage history of the Queen Maud Batholith, La Gorce Mountains, central Transantarctic Mountains. In *Proc. 8th Int. Symp. Antarctic Earth Sciences Wellington 1999* (eds Gamble, J. A., Skinner, D. N. B., Henrys, S. A.) 153–159 (Royal Society of New Zealand, 2002).
146. Gootee, B. & Stump, E. in *Antarctica* (eds Fütterer D. K., Damaske D., Kleinschmidt G., Miller H. & Tessensohn F.) 191–194 (Springer, 2006).
147. Barrett, P. J. in *Geology of Antarctica* (ed. Tingey, R. J.) 120–152 (Clarendon Press, 1991).
148. Ferraccioli, F., Armadillo, E., Jordan, T., Bozzo, E. & Corr, H. Aeromagnetic exploration over the East Antarctic Ice Sheet: a new view of the Wilkes Subglacial Basin. *Tectonophysics* **478**, 62–77 (2009).
149. Paxman, G. J. et al. Geology and Geomorphology of the Pensacola-Pole Basin, East Antarctica. *Geochem. Geophys. Geosyst.* **20**, 2786–2807 (2019).
150. Elliot, D. H. The Hanson Formation: a new stratigraphical unit in the Transantarctic Mountains, Antarctica. *Antarct. Sci.* **8**, 389–394 (1996).
151. Elliot, D. H. & Fleming, T. H. Occurrence and dispersal of magmas in the Jurassic Ferrar large igneous province, Antarctica. *Gondwana Res.* **7**, 223–237 (2004).
152. Burgess, S. D., Bowring, S. A., Fleming, T. H. & Elliot, D. H. High-precision geochronology links the Ferrar large igneous province with early-Jurassic ocean anoxia and biotic crisis. *Earth Planet. Sci. Lett.* **415**, 90–99 (2015).
153. Encarnación, J., Fleming, T. H., Elliot, D. H. & Eales, H. V. Synchronous emplacement of Ferrar and Karoo dolerites and the early breakup of Gondwana. *Geology* **24**, 535–538 (1996).
154. Cook, C. P. et al. Glacial erosion of East Antarctica in the Pliocene: A comparative study of multiple marine sediment provenance tracers. *Chem. Geol.* **466**, 199–218 (2017).
155. Adams, C. J. Geochronological studies of the Swanson Formation of Marie Byrd Land, West Antarctica, and correlation with northern Victoria Land, East Antarctica, and South Island, New Zealand. *N. Z. J. Geol. Geophys.* **29**, 345–358 (1986).
156. Yakymchuk, C. et al. Anatetic Reworking and Differentiation of Continental Crust Along the Active Margin of Gondwana: A Zircon Hf-O Perspective from West Antarctica (Geological Society London, Special Publication 383, 2013); <https://doi.org/10.1144/SP383.7>
157. Yakymchuk, C. et al. Paleozoic evolution of western Marie Byrd Land, Antarctica. *Bull. Geol. Soc. Am.* **127**, 1464–1484 (2015).
158. Simões Pereira, P. et al. The geochemical and mineralogical fingerprint of West Antarctica's weak underbelly: Pine Island and Thwaites glaciers. *Chem. Geol.* **550**, 119649 (2020).
159. Adams, C. J. Geochronology of granite terranes in the Ford Ranges, Marie Byrd Land, West Antarctica. *N. Z. J. Geol. Geophys.* **30**, 51–72 (1987).
160. LeMasurier, W. E. et al. *Volcanoes of the Antarctic Plate and Southern Ocean* Vol. 48 (American Geophysical Union, 1990).
161. Licht, K. J. et al. Evidence for extending anomalous Miocene volcanism at the edge of the East Antarctic craton. *Geophys. Res. Lett.* **45**, 3009–3016 (2018).
162. Brodie, J. W. A shallow shelf around Franklin Island in the Ross Sea, Antarctica. *N. Z. J. Geol. Geophys.* **2**, 108–119 (1959).
163. Lawyer, L., Lee, J., Kim, Y. & Davey, F. Flat-topped mounds in western Ross Sea: Carbonate mounds or subglacial volcanic features? *Geosphere* **8**, 645–653 (2012).
164. Di Vincenzo, G., Bracciali, L., Del Carlo, P., Panter, K. & Rocchi, S. 40Ar–39Ar dating of volcanic products from the AND-2A core (ANDRILL Southern McMurdo Sound Project, Antarctica): correlations with the Erebus Volcanic Province and implications for the age model of the core. *Bull. Volcanol.* **72**, 487–505 (2010).
165. Panter, K. S. et al. Melt origin across a rifted continental margin: a case for subduction-related metasomatic agents in the lithospheric source of alkaline basalt, NW Ross Sea, Antarctica. *J. Petrol.* **59**, 517–558 (2018).
166. McIntosh, W. C. 40Ar/39Ar geochronology of tephra and volcanic clasts in CRP-2A, Victoria Land Basin, Antarctica. *Terra Antarct.* **7**, 621–630 (2000).
167. LeMasurier, W. E. & Rocchi, S. Terrestrial record of post-Eocene climate history in Marie Byrd Land, West Antarctica. *Geogr. Ann., Ser. A* **87**, 51–66 (2005).
168. Rocchi, S., LeMasurier, W. E. & Di Vincenzo, G. Oligocene to Holocene erosion and glacial history in Marie Byrd Land, West Antarctica, inferred from exhumation of the Dorrel Rock intrusive complex and from volcano morphologies. *Bull. Geol. Soc. Am.* **118**, 991–1005 (2006).
169. LeMasurier, W. Shield volcanoes of Marie Byrd Land, West Antarctic rift: oceanic island similarities, continental signature, and tectonic controls. *Bull. Volcanol.* **75**, 726 (2013).
170. Behrendt, J. C. et al. Geophysical studies of the West Antarctic rift system. *Tectonics* **10**, 1257–1273 (1991).
171. McDougall, I. & Harrison, T. M. *Geochronology and Thermochronology by the 40Ar/39Ar Method* (Oxford Univ. Press, 1999).
172. Cherniak, D. J. & Watson, E. B. Pb diffusion in zircon. *Chem. Geol.* **172**, 5–24 (2001).
173. Morrison, A. D. & Reay, A. Geochemistry of Ferrar Dolerite sills and dikes at Terra Cotta Mountain, south Victoria Land, Antarctica. *Antarct. Sci.* **7**, 73–85 (1995).
174. Cox, S. C., Turnbull, I. M., Isaacs, M. J., Townsend, D. B. & Smith Lytle, B. *Geology of Southern Victoria Land, Antarctica* (Institute of Geological & Nuclear, 2012).
175. Ford, A. B. *Stratigraphy of the Layered Gabbroic Dufek Intrusion, Antarctica* (US Govt. Print. Off., 1976; <http://pubs.er.usgs.gov/publication/b1405D>)
176. Borg, S. G., Depaolo, D. J. & Smith, B. M. Isotopic structure and tectonics of the central Transantarctic Mountains. *J. Geophys. Res. Solid Earth* **95**, 6647–6667 (1990).
177. Cox, S. C., Parkinson, D. L., Allibone, A. H. & Cooper, A. F. Isotopic character of Cambro-Ordovician plutonism, southern Victoria Land, Antarctica. *N. Z. J. Geol. Geophys.* **43**, 501–520 (2000).
178. Gunner, J. *Isotopic and Geochemical Studies of the Pre-Devonian Basement Complex, Beardmore Glacier Region, Antarctica* (Ohio State Univ. Institute of Polar Studies Report No. 41, 1976).
179. Roy, M., van de Flieerd, T., Hemming, S. R. & Goldstein, S. L. 40Ar/39Ar ages of hornblende grains and bulk Sm/Nd isotopes of circum-Antarctic glacio-marine sediments: Implications for sediment provenance in the Southern Ocean. *Chem. Geol.* **244**, 507–519 (2007).
180. Behrendt, J. C. The aeromagnetic method as a tool to identify Cenozoic magmatism in the West Antarctic Rift System beneath the West Antarctic Ice Sheet—A review; Thiel subglacial volcano as possible source of the ash layer in the WAISCORE. *Tectonophysics* **585**, 124–136 (2013).
181. Lough, A. C. et al. Seismic detection of an active subglacial magmatic complex in Marie Byrd Land, Antarctica. *Nat. Geosci.* **6**, 1031–1035 (2013).
182. Schroeder, D. M., Blankenship, D. D., Young, D. A. & Quartini, E. Evidence for elevated and spatially variable geothermal flux beneath the West Antarctic Ice Sheet. *Proc. Natl. Acad. Sci. USA* **111**, 9070–9072 (2014).
183. Ehrmann, W. U., Melles, M., Kuhn, G. & Grobe, H. Significance of clay mineral assemblages in the Antarctic Ocean. *Mar. Geol.* **107**, 249–273 (1992).
184. Fagel, N. Clay minerals, deep circulation and climate. *Proxies Late Cenozoic Paleceanogr.* **1**, 139–184 (2007).
185. Kristoffersen, Y., Strand, K., Vorren, T., Harwood, D. & Webb, P. Pilot shallow drilling on the continental shelf, Dronning Maud Land, Antarctica. *J. Antarct. Sci.* **4**, 463–470 (2000).
186. Ehrmann, W. et al. Provenance changes between recent and glacial-time sediments in the Amundsen Sea embayment, West Antarctica: clay mineral assemblage evidence. *Antarct. Sci.* **23**, 471–486 (2011).
187. Hillenbrand, C. D., Grobe, H., Diekmann, B., Kuhn, G. & Fütterer, D. K. Distribution of clay minerals and proxies for productivity in surface sediments of the Bellingshausen and Amundsen seas (West Antarctica)—Relation to modern environmental conditions. *Mar. Geol.* **193**, 253–271 (2003).
188. Klages, J. P. et al. Temperate rainforests near the South Pole during peak Cretaceous warmth. *Nature* **580**, 81–86 (2020).
189. Zonneveld, K. A. F., Bockelmann, F. & Holzwarth, U. Selective preservation of organic-walled dinoflagellate cysts as a tool to quantify past net primary production and bottom water oxygen concentrations. *Mar. Geol.* **237**, 109–126 (2007).
190. Prebble, J. G., Hannah, M. J. & Barrett, P. J. Changing Oligocene climate recorded by palynomorphs from two glacio-eustatic sedimentary cycles, Cape Roberts Project, Victoria Land Basin, Antarctica. *Palaeogeogr. Palaeoclimatol. Palaeoecol.* **231**, 58–70 (2006).
191. Kulhanek, D. K. et al. Revised chronostratigraphy of DSDP Site 270 and late Oligocene to early Miocene paleoecology of the Ross Sea sector of Antarctica. *Global Planet. Change* **178**, 46–64 (2019).
192. Feakins, S., Warny, S. & Lee, J. E. Hydrologic cycling over Antarctica during the middle Miocene warming. *Nat. Geosci.* **5**, 557–560 (2012).
193. De Santis, L., Prato, S., Brancolini, G., Lovo, M. & Torelli, L. The Eastern Ross Sea continental shelf during the Cenozoic: implications for the West Antarctic ice sheet development. *Global Planet. Change* **23**, 173–196 (1999).
194. Ford, A. B. & Barrett, P. J. Basement rocks of the south-central Ross Sea, Site 270, DSDP Leg 28. *Initial Rep. Deep Sea Drill. Proj.* **28**, 861–868 (1975).
195. Goldich, S. S., Treves, S. B., Suhr, N. H. & Stuckless, J. S. Geochemistry of the Cenozoic volcanic rocks of Ross Island and vicinity, Antarctica. *J. Geol.* **83**, 415–435 (1975).
196. Tulacyk, S., Kamb, B., Scherer, R. P. & Engelhardt, H. F. Sedimentary processes at the base of a West Antarctic ice stream; constraints from textural and compositional properties of subglacial debris. *J. Sediment. Res.* **68**, 487–496 (1998).
197. Rosengqvist, I. T. Origin and mineralogy glacial and interglacial clays of southern Norway. *Clays Clay Miner.* **23**, 153–159 (1975).
198. Blum, J. D. & Erel, Y. Rb/Sr isotope systematics of a granitic soil chronosequence: The importance of biotite weathering. *Geochim. Cosmochim. Acta* **61**, 3193–3204 (1997).
199. Eisenhauer, A. et al. Grain size separation and sediment mixing in Arctic Ocean sediments: evidence from the strontium isotope systematic. *Chem. Geol.* **158**, 173–188 (1999).

Article

200. Haran, T. MODIS Mosaic of Antarctica 2008–2009 (MOA2009) Image Map, Version 1. Boulder, Colorado, USA., NASA National Snow and Ice Data Center Distributed Active Archive Center, <https://doi.org/10.7265/N5KP8037> (2014).

Acknowledgements This research used data and samples provided by the International Ocean Discovery Program (IODP), which is sponsored by the US National Science Foundation (NSF) and participating countries under the management of Joint Oceanographic Institutions. J.W.M. was supported by a NERC DTP studentship (grant number NE/L002515/1). Neodymium and Sr isotope analysis and U-Pb dating of detrital zircons was funded through NERC UK IODP grant NE/R018219/1. Clast counts performed by L.Z., F.T. and M.P. and the participation of L.D. and F.C. was funded by the Italian National Antarctic Research Program (PNRA, *Programma Nazionale Ricerche in Antartide*), grant numbers PNRA18-00233, PNRA16-00016 and PNRA18-00002. R.M.M. was supported by Royal Society Te Apārangi Marsden Fund (18-VUW-089). R.M.M., J.G.P. and R.L. were supported by the New Zealand Ministry for Business Innovation and Employment grant ANTA1801. P.V. was partially funded by NERC Standard Grant NE/T001518/1. L.F.P. has been funded by the European Union's Horizon 2020 research and innovation programme under the Marie Skłodowska-Curie grant agreement no. 792773 WAMSISe. T.E.v.P. has been funded by NERC grants NE/R018235/1 and NE/T012285/1. D.K.K. was supported by the IODP JOIDES Resolution Science Operator and National Science Foundation (grant numbers OCE-1326927 and OPP-2000995). A.E.S. and I.B. were supported by the US Science Support Program. Southern Transantarctic Mountain rock samples for Nd and Sr isotope analysis were provided by the Polar Rock Repository with support from the National Science Foundation, under Cooperative Agreement OPP-1643713. We thank B. Coles, K. Kreissig and P. Simões Pereira for technical support. We also thank the numerous scientists who collected invaluable site survey data and developed the proposals and hypotheses that ultimately led to IODP Expedition 374. Expedition 374 was conducted under Antarctic

Conservation Act Permit Number: ACA 2018-027 (permit holder: Bradford Clement, JRSO, IODP, TAMU, College Station, TX 77845).

Author contributions J.W.M., T.v.d.F., R.M.M., L.D.S. and A.E.S. designed the research in collaboration with the entire IODP Expedition 374 science party. J.W.M. conducted the Nd and Sr isotope analyses. L.Z., F.T. and M.P. performed the clast counts. J.W.M., P.V. and A.C. produced the zircon U-Pb data. F.B. and V.B.R. collected the clay mineralogy data. F.S., J.G.P. and C.B. performed the palynological counts and interpretations. S.R.H. provided the hornblende $^{40}\text{Ar}/^{39}\text{Ar}$ data. K.J.L. provided guidance on geochronology interpretations. L.F.P., F.C. and L.D.S. calculated the sediment volume estimate. R.L., R.M.M., T.E.v.P., D.H., D.K.K. and E.M.G. improved the shipboard age model. N.B.S. and S.R.M. conducted the astrochronological analyses. D.K.K. provided the XRF data. E.G. and B.K. helped integrate sediment provenance data with numerical modelling. I.B., G.K. and J.P.D. advised on specific technical aspects of the manuscript. J.W.M. created the figures and wrote the text with assistance from all authors and particular guidance from T.v.d.F., C.D.H., E.G. and M.J.S. All Expedition 374 scientists contributed to the collection of shipboard datasets and the interpretations of the data.

Competing interests The authors declare no competing interests.

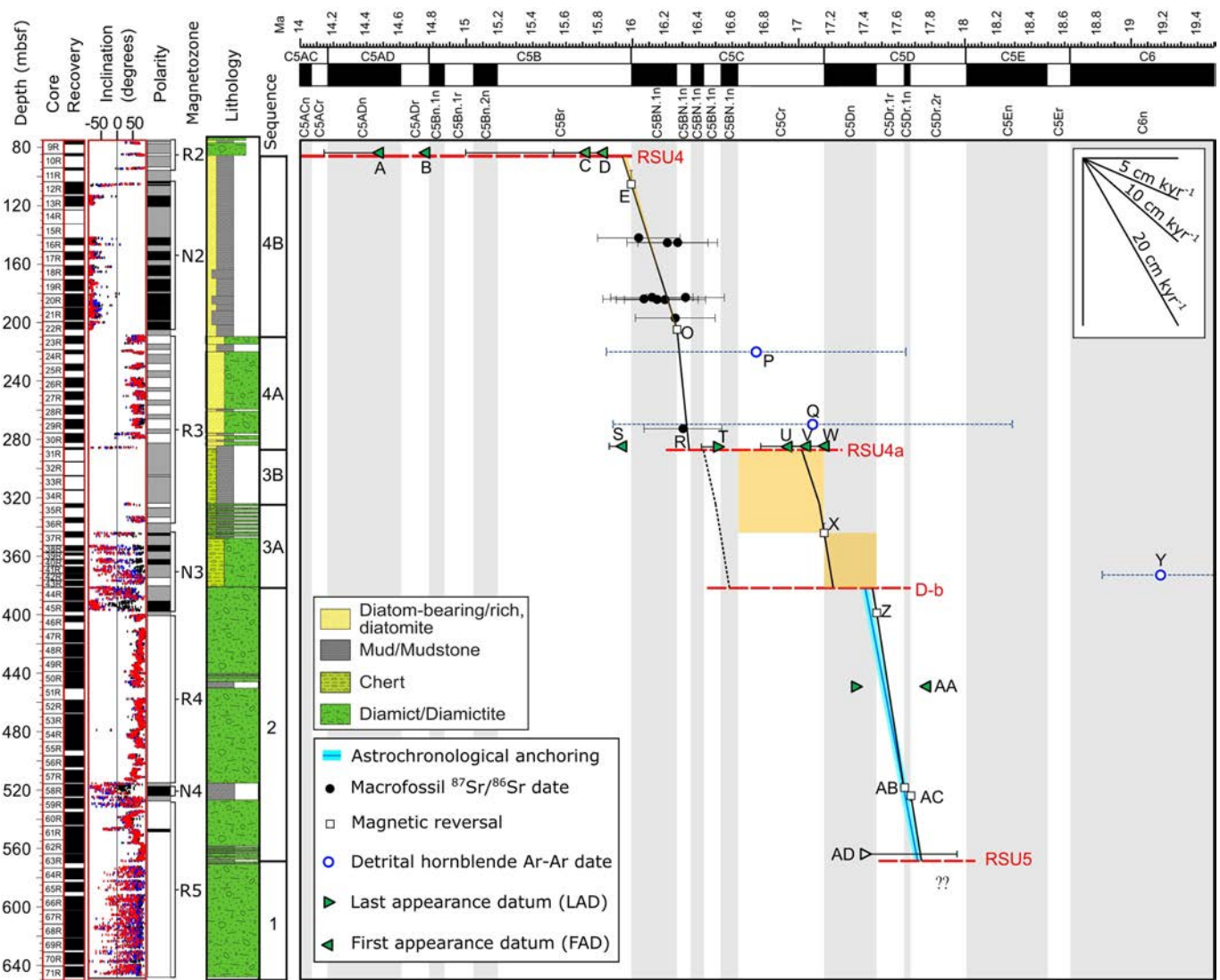
Additional information

Supplementary information The online version contains supplementary material available at <https://doi.org/10.1038/s41586-021-04148-0>.

Correspondence and requests for materials should be addressed to J. W. Marschalek.

Peer review information *Nature* thanks Patrick Blaser, Maria Fernanda Sanchez-Goni, Kenneth Miller and the other, anonymous, reviewer(s) for their contribution to the peer review of this work. Peer reviewer reports are available.

Reprints and permissions information is available at <http://www.nature.com/reprints>.

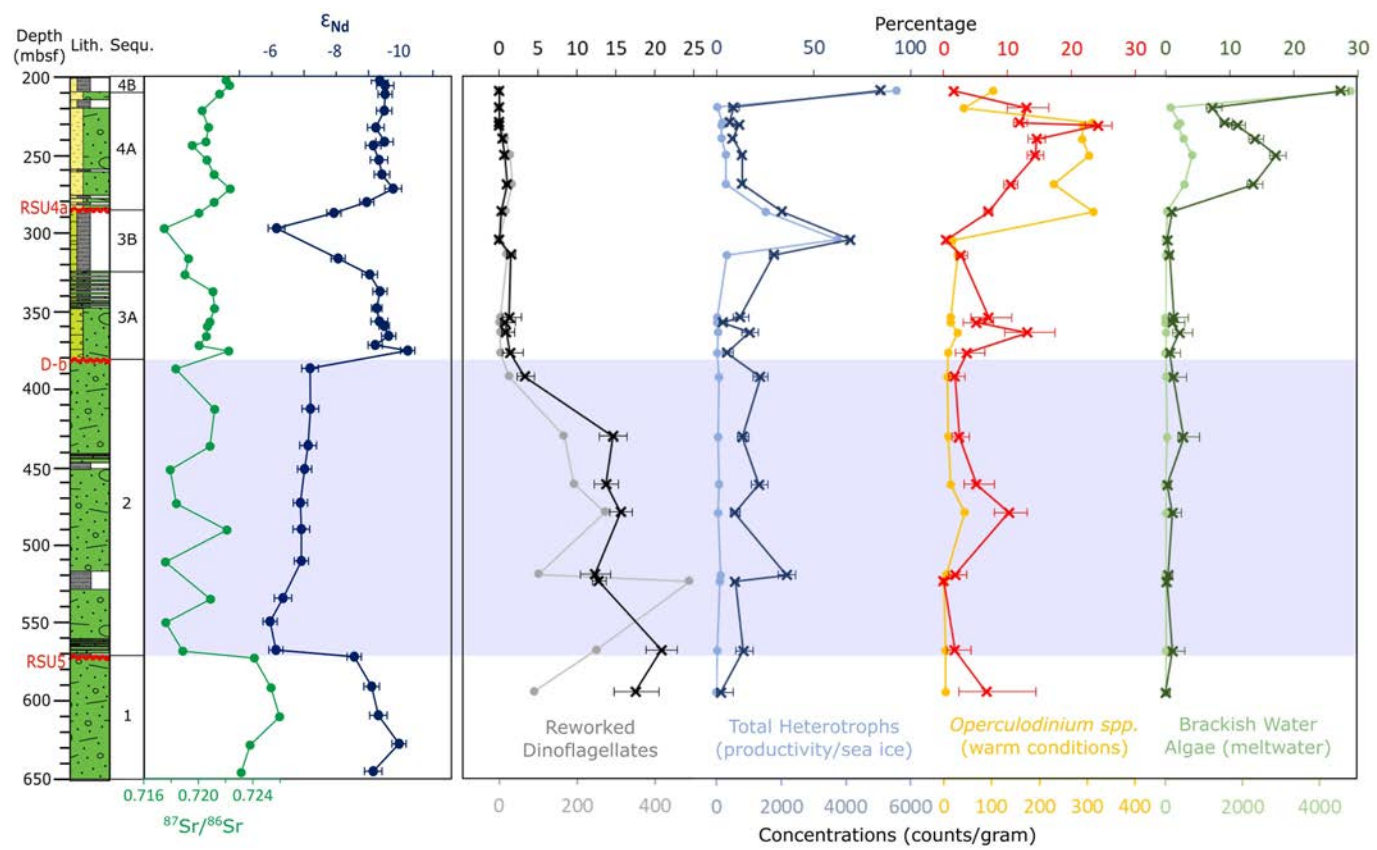


Extended Data Fig. 1 | Age model constraints below 75 mbsf at Site U1521.

From left to right are: depth (metres below sea floor), core number, core recovery (black = recovered), inclination before and after 10 and 20 mT demagnetisation (black, blue and red points, successively), and corresponding polarity interpretations (black = normal, white = reversed, grey = no interpretation). Note that the polarity interpretations have been simplified compared to those in the cruise report²⁶, with small uncertainties related to core gaps removed. Note Site U1521 is in the Southern Hemisphere. The

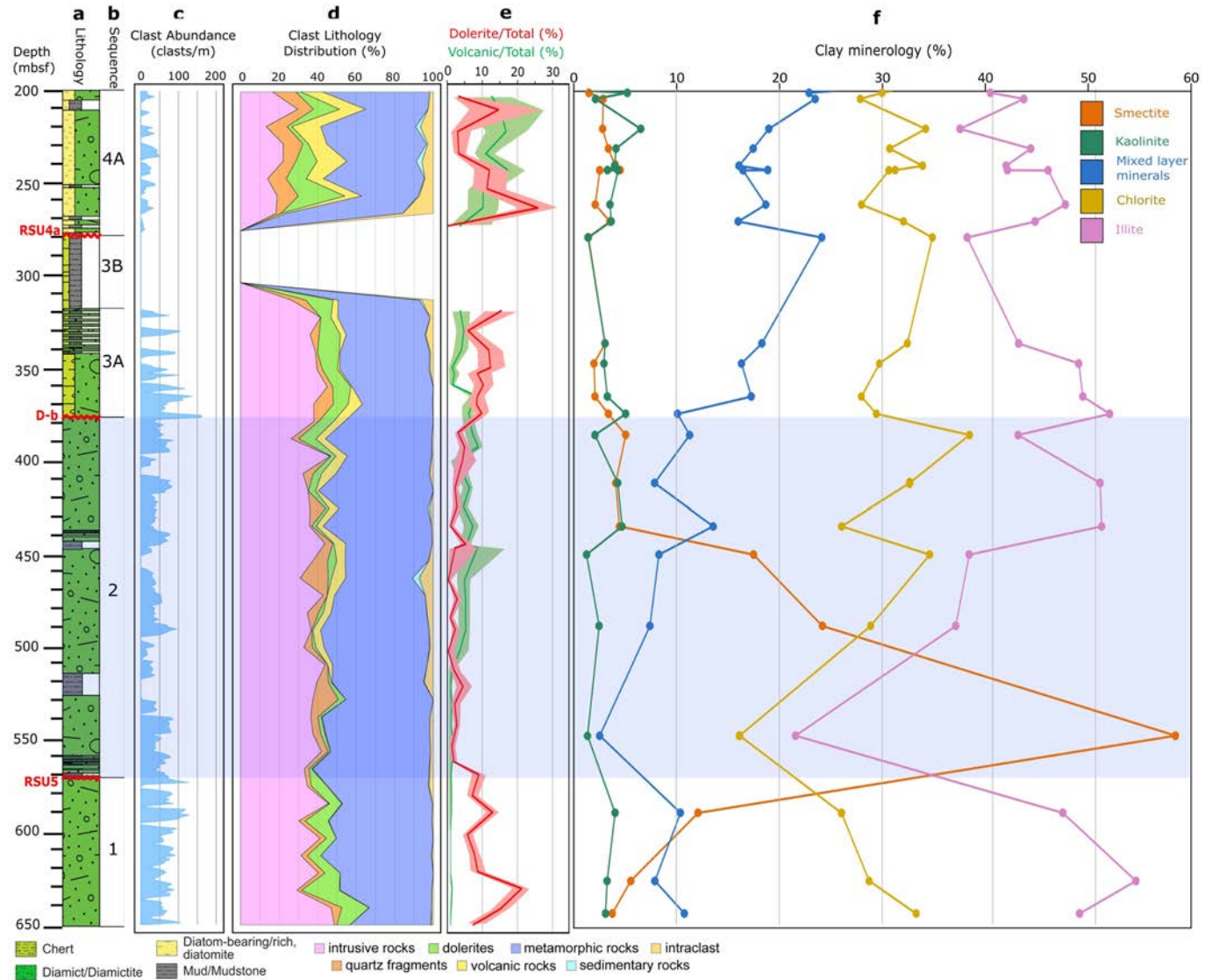
geomagnetic polarity timescale⁴⁹ is shown across the top of the plot. The orange shaded regions indicate uncertainties in our age model and the dashed line marks an alternative line of correlation for Sequence 3. The blue line indicates the age model for Sequence 2 based on our astrochronological analyses, with the light blue shading indicating the -20 kyr uncertainty associated with the phase relationship between clast abundances and obliquity. This astrochronological anchoring agrees closely with linear interpolations between magnetostratigraphic tie points (black line).

Article



Extended Data Fig. 2 | Selected palynological counts compared to strontium and neodymium isotope data. Palynological data are reported as percentages (crosses) and counts/gram (circles). The blue shaded area

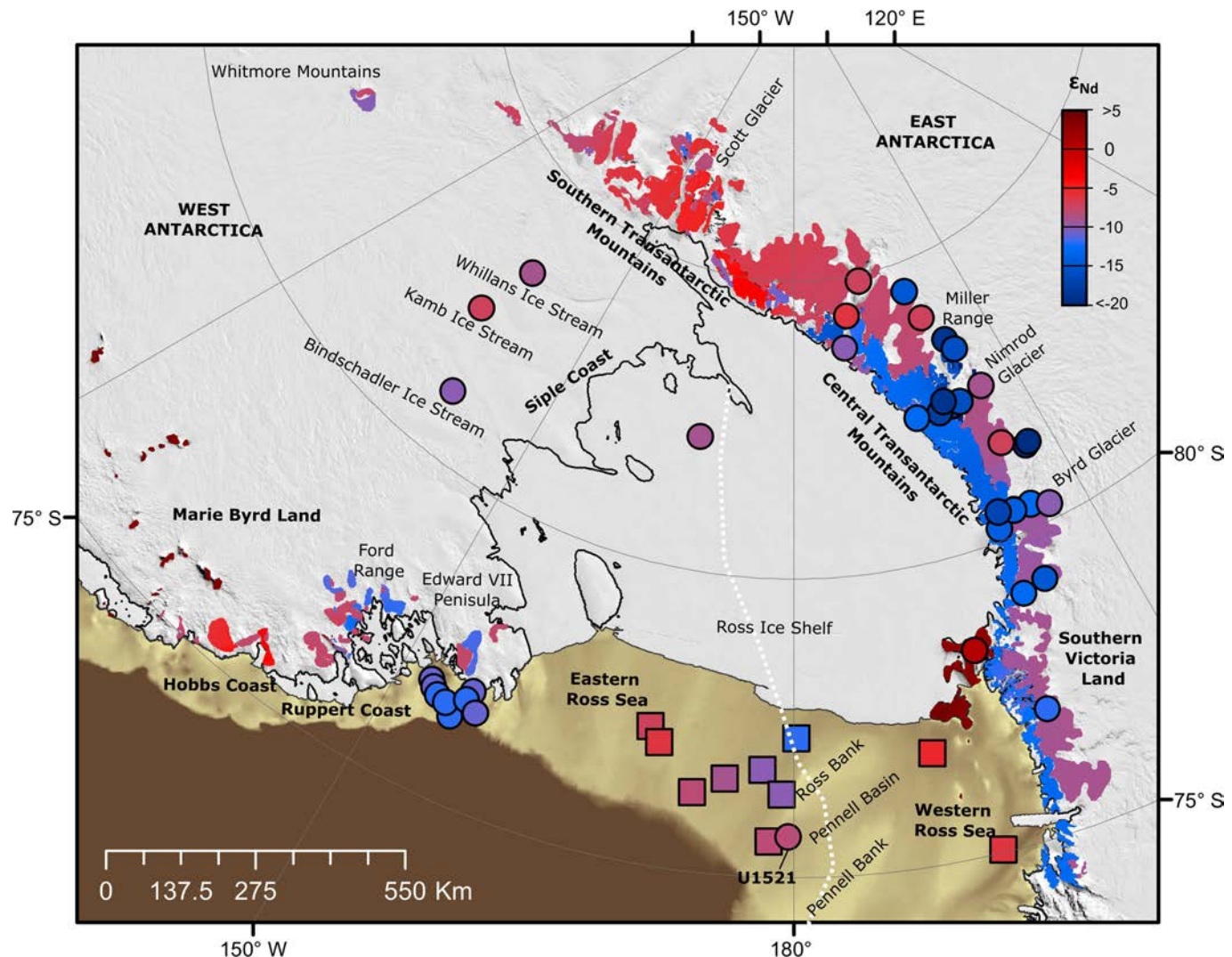
represents Sequence 2, which is interpreted as consisting of sediments with a West Antarctic provenance. Error bars indicate a 95% confidence interval⁴⁸.



Extended Data Fig. 3 | Down-core clast and clay mineral distribution.

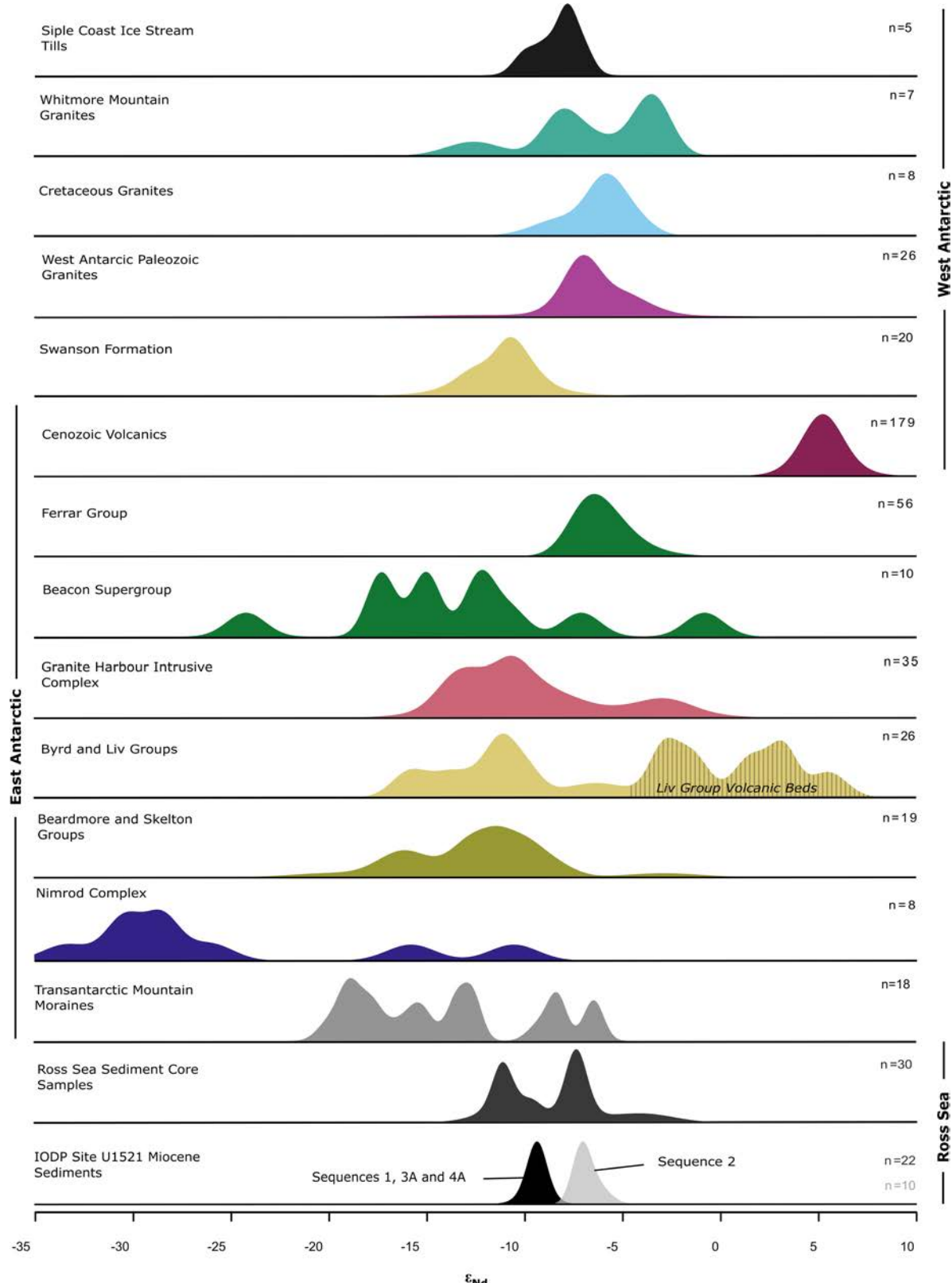
The blue shaded area highlights Sequence 2, which is interpreted to consist of sediments with a West Antarctic provenance. **a)** Core lithology. **b)** Chronostratigraphic sequences. **c)** Clast abundance. **d)** Percentages of

different clast lithologies. **e)** Ratio between dolerite and total number of clasts (red) and volcanic rocks and total number of clasts (green), with 95% confidence interval shown as pale shading⁴⁸. **f)** Clay mineral abundances.



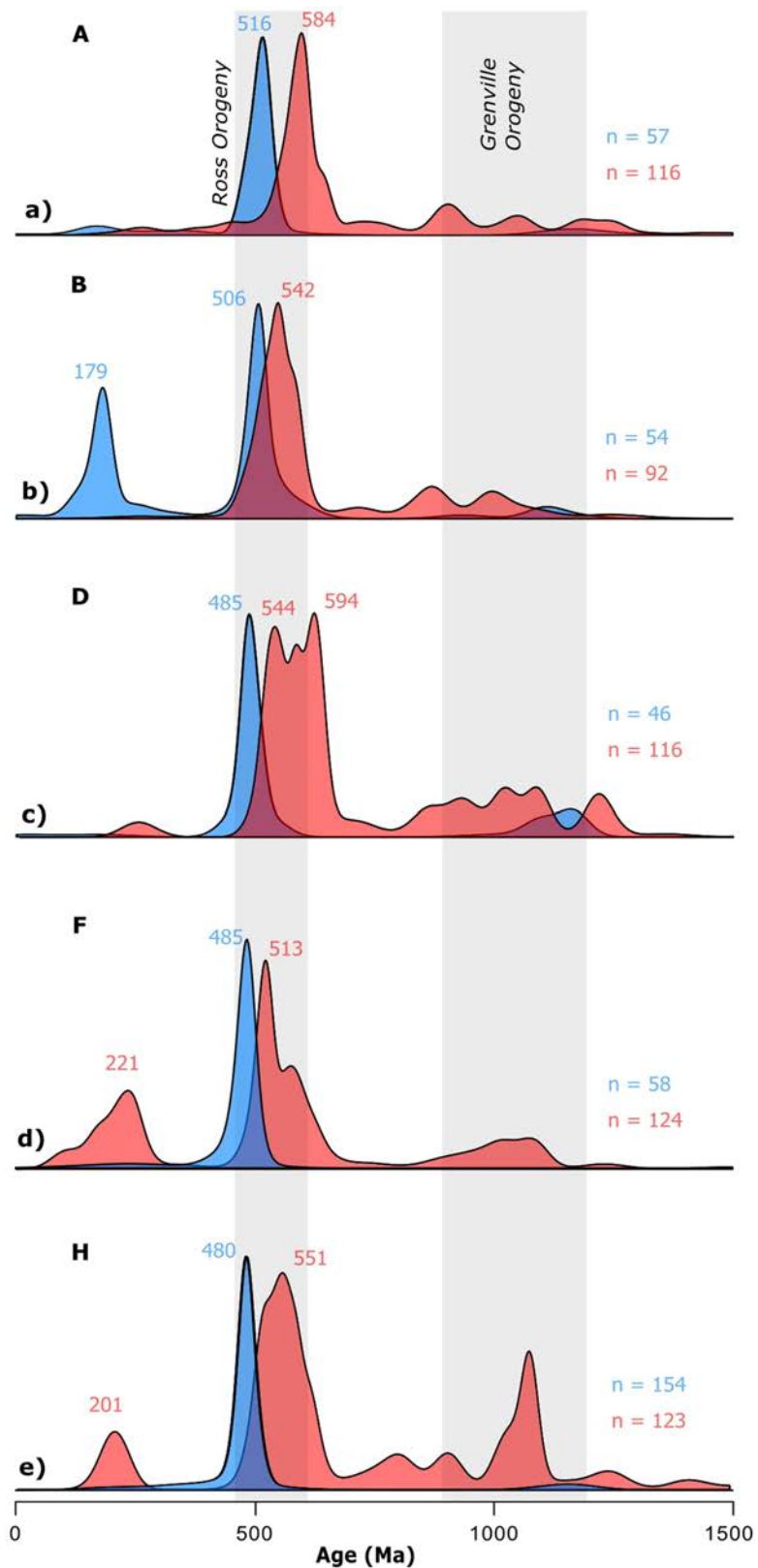
Extended Data Fig. 4 | Map of approximate ϵ_{Nd} values in rocks and offshore sediments from around the Ross Sea embayment. Epsilon Nd values are overlain on MODIS imagery²⁰⁰ and the BedMachine Antarctica V1 modern bed topography^{43,44}, with the MEASUREs grounding line and ice sheet margin shown^{45,46}. The approximate boundary between West and East Antarctic lithosphere is shown using a white dashed line⁴⁷. Modern/late Holocene and terrestrial till samples are represented by circles with the same colour bar^{28,30,55}. Although ice flow patterns have changed since their deposition, Last Glacial

Maximum tills in offshore sediments are also plotted as squares to improve spatial coverage²⁸. Individual samples and references are reported in Supplementary Table 1. The bedrock map was produced by Kriging between sample locations within a group, then masking to the outcrop area. Beacon and Ferrar Group (Fig. 1) rocks are often not differentiated in geological mapping, but are roughly equal volumetrically¹³⁶, with the uppermost Beacon Supergroup formations having a Ferrar-like isotopic signature¹³⁹. We hence assume a 60% Ferrar, 40% Beacon mixture is representative.



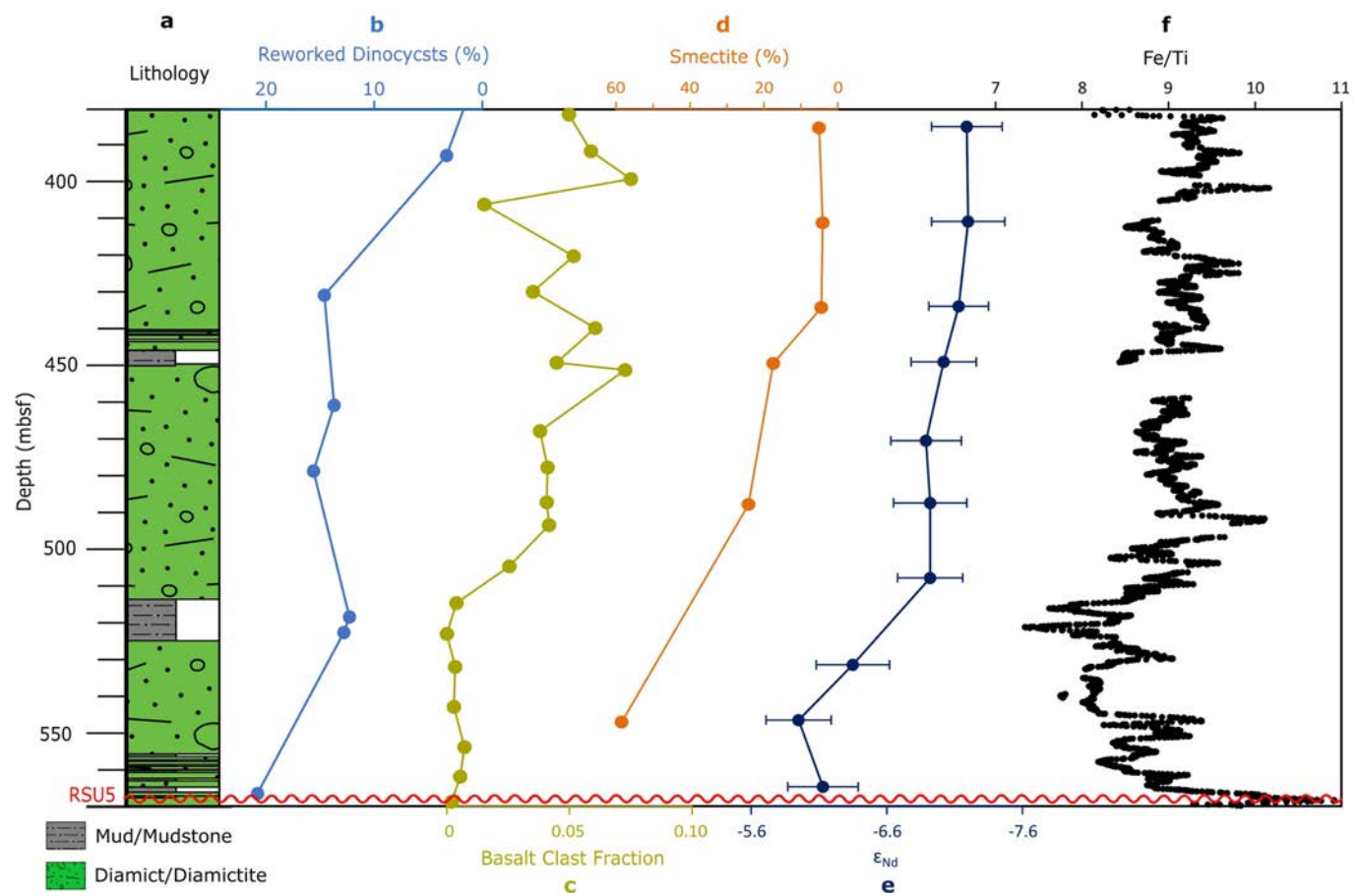
Extended Data Fig. 5 | Kernel density estimate plots for literature measurements of rock ϵ_{Nd} compared to measurements on fine-grained Miocene detritus from Site U1521. For references and a list of all the data, see

Supplementary Table 1. The height of the curve indicates the density of measurements and n the total number of samples analysed. Colour scheme is identical to Fig. 1, with sediments in grey.



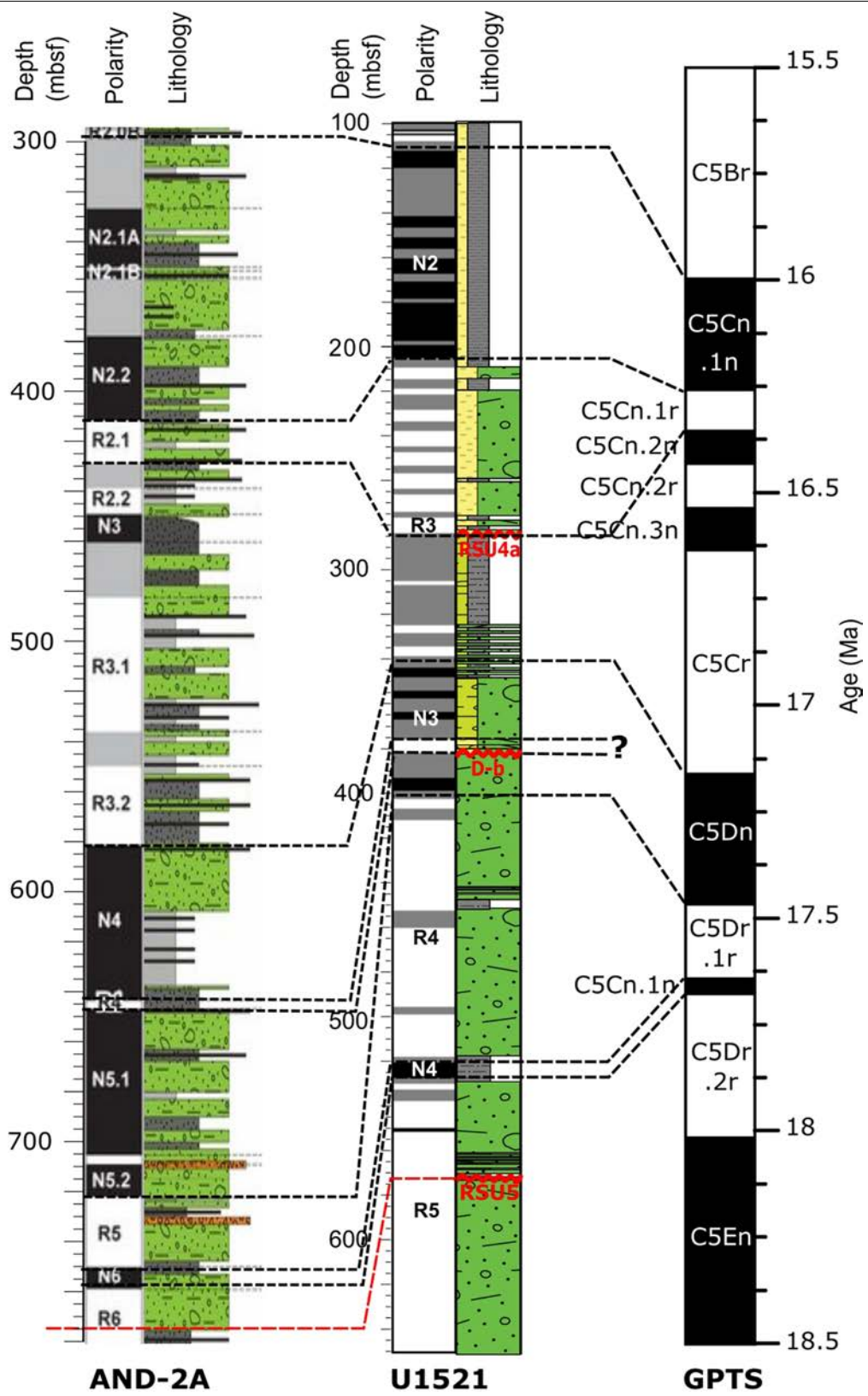
Extended Data Fig. 6 | Kernel density estimates for hornblende $^{40}\text{Ar}/^{39}\text{Ar}$ ages compared to zircon U-Pb ages younger than 1500 Ma. The two dating methods are shown in red and blue, respectively. Bold letters correspond with

those in Fig. 3. The positions of major peaks and number of grains analysed are labelled in the corresponding colours. Stratigraphic position is shown in Fig. 2.



Extended Data Fig. 7 | Close up of the Site U1521 interval with a West Antarctic provenance. The stratigraphic log (a) is displayed alongside the percentage of reworked dinocysts (b), basalt clast fraction (c), relative

abundance of smectite (d), Nd isotope data (e) and Fe/Ti ratios determined by X-ray fluorescence scanning (f).



Extended Data Fig. 8 | Correlation of Site U1521 magnetostratigraphic tie points. Shown are correlations between the AND-2A record¹¹, Site U1521²⁶ and the GPTS⁴⁹.

Extended Data Table 1 | Age tie points for Site U1521 below 75 mbsf

Depth (mbsf)	Depth Error	Event	Event Description	Type	Age (Ma)	Age Error	References	Notes
84.99	85.55	A	<i>Denticulopsis simonsenii</i>	FAD	14.48	14.14	89, 90	
84.99	85.72	B	<i>Denticulopsis hyalina</i>	FAD	14.76	14.73	89, 90	
84.99	85.55	C	<i>D. lauta</i>	FAD	15.72	14.99	89, 90	
84.99	85.55	D	<i>A. ingens</i>	FAD	15.83	15.52	89, 90	
85.34			RSU4	Unconformity	15.83-14.48		23	
105.9	± 0.4	E	C5Br/C5Cn.1n	MPR	15.994		49	
141.92		F	Shell Fragments	$^{87}\text{Sr}/^{86}\text{Sr}$ (Bivalve)	16.039	± 0.25		
145.135		G	Shell Fragments	$^{87}\text{Sr}/^{86}\text{Sr}$ (Bivalve)	16.211	± 0.24		
145.135		H	Shell Fragments	$^{87}\text{Sr}/^{86}\text{Sr}$ (Bivalve)	16.272	± 0.24		
182.7		I	Shell Fragments	$^{87}\text{Sr}/^{86}\text{Sr}$ (Bivalve)	16.117	± 0.25		
182.71		J	Shell Fragments	$^{87}\text{Sr}/^{86}\text{Sr}$ (Bivalve)	16.319	± 0.23		
183.825		K	Shell Fragments	$^{87}\text{Sr}/^{86}\text{Sr}$ (Bivalve)	16.071	± 0.25		
184.215		L	Shell Fragments	$^{87}\text{Sr}/^{86}\text{Sr}$ (Bivalve)	16.196	± 0.24		
184.215		M	Shell Fragments	$^{87}\text{Sr}/^{86}\text{Sr}$ (Bivalve)	16.149	± 0.25		
196.785		N	Shell Fragments	$^{87}\text{Sr}/^{86}\text{Sr}$ (Bivalve)	16.257	± 0.24		
207.0	± 2.0	O	C5Cn.1n/C5Cn.1r	MPR	16.261		49	
220.23	± 0.20	P	Hornblende grain (150-300 µm)	$^{40}\text{Ar}/^{39}\text{Ar}$ date	16.740	± 0.90		
270.03	± 0.20	Q	Hornblende grain (150-300 µm)	$^{40}\text{Ar}/^{39}\text{Ar}$ date	17.080	± 1.20		
272.65		R	Shell Fragments	$^{87}\text{Sr}/^{86}\text{Sr}$ (Bivalve)	16.304	± 0.23		
286.1	Opal CT	S	<i>N. grosssepunctata</i>	FAD	15.94	15.87	89, 90	
286.1	Opal CT	T	<i>F. maleinterpretaria</i>	LAD	16.41	16.5	88, 89, 90	Incomplete
286.1	Opal CT	U	<i>S. cheethamii</i>	FAD	16.94	N/A	90	
286.1	Opal CT	V	<i>D. maccollumii</i>	FAD	17.05	16.77	89, 90	
286.1	Opal CT	W	<i>N. 17 Schrader</i>	FAD	17.16	16.94	89, 90	
286.30			RSU4a	Unconformity	16.3 - 17		23	
341.0	± 3.6	X	C5Cr/C5Dn	MPR	17.154		49	
373.58	± 0.20	Y	Hornblende grain (150-300 µm)	$^{40}\text{Ar}/^{39}\text{Ar}$ date	19.17	± 0.35		Grain likely reworked
380.04			D-b	Unconformity	17.25 - 17.45		23	
398.85	± 1.65	Z	C5Dn/C5Dr.1r	MPR	17.466		49	
450.52	450.57	AA	<i>Thalassiosira sp. cf. T. bukryi</i>	Occurrence	17.7-17.4		89, 93	
567.95			RSU5	Unconformity	18.6-17.8		11, 23	

FAD: First Appearance Datum, LAD: Last Appearance Datum. Depth errors for the biostratigraphic datums reflect the position of the first downhole sample in which the reported species was not observed. We cannot exclude the possibility that the true first observation occurs between this sample and that reported as the FAD. Opal-CT indicates that the lowermost occurrence is uncertain due to poor preservation below the Opal-CT transition (~286.1 mbsf). Age errors for the biostratigraphic events are given as the maximum and minimum reported ages based on hybrid range models^{89,90}. Magnetic Polarity Reversals (MPR) depths are given as midpoints between samples with differing polarities, with the depth error indicating the distance to these samples.

Article

Extended Data Table 2 | Values used in the erosion rate calculation

	Median Erosion Estimate	Minimum Erosion Estimate	Maximum Erosion Estimate
Sediment Volume (km ³)	123,627	111,077	136,177
Mean Porosity	0.436	0.499	0.374
Terrigenous Fraction	0.95	0.9	1
Catchment Area (km ²)	759,640	911,569	607,712
Catchment Mean Erosion (m)	87.14	54.97	140.26
Duration (years)	317,416	337,416	297,416
Mean Erosion Rate (mm yr ⁻¹)	0.275	0.163	0.472